



Genesis and Impulsive Evolution of the 2017 September 10 Coronal Mass Ejection

Astrid M. Veronig^{1,2} , Tatiana Podladchikova³ , Karin Dissauer¹ , Manuela Temmer¹ , Daniel B. Seaton^{4,5} ,
David Long⁶ , Jingnan Guo⁷, Bojan Vršnak⁸, Louise Harra⁶ , and Bernhard Kliem⁹

¹ Institute of Physics, University of Graz, Austria; astrid.veronig@uni-graz.at

² Kanzelhöhe Observatory for Solar and Environmental Research, University of Graz, Austria

³ Skolkovo Institute of Science and Technology, Moscow, Russia

⁴ Cooperative Institute for Research in Environmental Science, University of Colorado at Boulder, Boulder, CO, USA

⁵ National Centers for Environmental Information, National Oceanic and Atmospheric Administration, Boulder, CO, USA

⁶ UCL-Mullard Space Science Laboratory, Holmbury St. Mary, Dorking, Surrey, UK

⁷ Institut für Experimentelle und Angewandte Physik, University of Kiel, Germany

⁸ Hvar Observatory, Faculty of Geodesy, University of Zagreb, Croatia

⁹ Institute of Physics and Astronomy, University of Potsdam, Germany

Received 2018 July 5; revised 2018 October 18; accepted 2018 October 21; published 2018 November 29

Abstract

The X8.2 event of 2017 September 10 provides unique observations to study the genesis, magnetic morphology, and impulsive dynamics of a very fast coronal mass ejection (CME). Combining *GOES-16/SUVI* and *SDO/AIA* EUV imagery, we identify a hot ($T \approx 10\text{--}15$ MK) bright rim around a quickly expanding cavity, embedded inside a much larger CME shell ($T \approx 1\text{--}2$ MK). The CME shell develops from a dense set of large AR loops ($\gtrsim 0.5R_{\odot}$) and seamlessly evolves into the CME front observed in *LASCO C2*. The strong lateral overexpansion of the CME shell acts as a piston initiating the fast EUV wave. The hot cavity rim is demonstrated to be a manifestation of the dominantly poloidal flux and frozen-in plasma added to the rising flux rope by magnetic reconnection in the current sheet beneath. The same structure is later observed as the core of the white-light CME, challenging the traditional interpretation of the CME three-part morphology. The large amount of added magnetic flux suggested by these observations explains the extreme accelerations of the radial and lateral expansion of the CME shell and cavity, all reaching values of $5\text{--}10$ km s⁻². The acceleration peaks occur simultaneously with the first *RHESSI* 100–300 keV hard X-ray burst of the associated flare, further underlining the importance of the reconnection process for the impulsive CME evolution. Finally, the much higher radial propagation speed of the flux rope in relation to the CME shell causes a distinct deformation of the white-light CME front and shock.

Key words: Sun: activity – Sun: corona – Sun: coronal mass ejections (CMEs) – Sun: flares

Supporting material: animations

1. Introduction

Coronal mass ejections (CMEs) are large-scale structures of magnetized plasma that are expelled from the Sun with speeds ranging from ~ 100 up to about 3500 km s⁻¹ (St. Cyr et al. 1999; Gopalswamy et al. 2009), driven by magnetic forces (e.g., reviews by Forbes et al. 2006; Chen & Wu 2011; Green et al. 2018). They are the most energetic events in our solar system, being associated with energy releases of up to $\sim 10^{32}$ erg (Vourlidas et al. 2010; Emslie et al. 2012). Fast CMEs are often associated with EUV waves, which are widely believed to be low coronal signatures of large-amplitude fast-mode magnetosonic waves or shocks (e.g., reviews by Patsourakos & Vourlidas 2012; Liu & Ofman 2014; Warmuth 2015; Long et al. 2017). When the interplanetary counterpart of a CME, the ICME, and its associated shock reach Earth, they may induce strong geomagnetic storms, with the storm strength mainly depending on the southward (B_z) component of the ICME's magnetic field and on its impact speed (Tsurutani et al. 1988, 1992; Gonzalez et al. 1994). Recent studies, in particular owing to the multispacecraft in situ observations of the *STEREO* satellites, revealed the production of widespread solar energetic particles (SEPs), which seem to be able to fill

the whole heliosphere (Dresing et al. 2012; Gómez-Herrero et al. 2015; Lario et al. 2016). It is understood that these extreme cases of widespread SEP events are related to specific properties of the CME and its associated shock close to the Sun (extended source region) and/or to perpendicular particle transport processes in interplanetary space (e.g., Dresing et al. 2014). Thus, the origin and early evolution of CMEs close to the Sun, their interplanetary propagation, and their interaction processes with the Earth magnetosphere are all key aspects in the understanding and prediction of extreme space weather events (e.g., Koskinen et al. 2017).

CMEs observed in white-light coronagraphs often reveal a three-part structure: a leading bright front followed by a dark cavity (void) and an embedded bright core (Illing & Hundhausen 1986). The bright front is a shell of enhanced density, due to compressed and piled-up material ahead of the erupting structure. The dark cavity and the bright core are generally interpreted as manifestations of a magnetic flux rope, i.e., a coherent helical magnetic structure with the field lines wrapping around the central axis (e.g., Low & Hundhausen 1995). The flux rope may fill the whole volume of the dark coronal cavity, and thus the cavity may outline the flux rope's cross section in the plane of the sky (Chen et al. 1997; see also the review by Cheng et al. 2017). The bright core is usually interpreted as corresponding to the cool and dense prominence material that is suspended in the magnetic dips at the bottom of the twisted flux rope (e.g., Dere et al. 1999; Gibson et al. 2006). However, Howard et al. (2017) challenged this view,



Original content from this work may be used under the terms of the [Creative Commons Attribution 3.0 licence](https://creativecommons.org/licenses/by/3.0/). Any further distribution of this work must maintain attribution to the author(s) and the title of the work, journal citation and DOI.

suggesting that the bright core represents the erupting flux rope with prominence material contributing to the emission only in a minority of events. Vourlidas et al. (2013) pointed out that the CME front in the classical three-part structure may actually reveal a “two-front” morphology. The bright loop-like front observed in the coronagraphs corresponds to the piled-up material ahead of the erupting structure. In addition, also a fainter outer front may be visible in the white-light coronagraph images (first reported in Vourlidas et al. 2003, and reported in a number of events thereafter) as a result of the density enhancement by the shock that is driven by quickly accelerating CMEs.

Recently, the early evolution of CMEs, their flux ropes, and cavities in the inner corona have become accessible in the high-cadence multiband EUV observations from *STEREO* EUVI and *Solar Dynamics Observatory* (*SDO*) AIA. This is an important height range, where many CMEs appear to form and to undergo their impulsive acceleration phase (Patsourakos et al. 2010a, 2010b; Temmer et al. 2010; Bein et al. 2011; Cheng et al. 2011). Several studies have shown that hot flux ropes may be enclosed in a dark cavity observed in cool EUV passbands, showing plasma at typical quiet coronal temperatures (Cheng et al. 2011, 2013; Zhang et al. 2012). A statistical study of eruptions observed in the EUV by Nindos et al. (2015) revealed that about half of the events exhibit a hot flux rope.

In general, CMEs observed in the coronagraph field of view (FOV); i.e., beyond several solar radii reveal a self-similar expansion, i.e., the radial expansion and lateral expansion develop at the same rate (Schwenn et al. 2005). Recent studies of CME and cavity evolution in high-cadence EUV imagery report fast lateral overexpansion of CMEs low in the corona, i.e., the radius (width) of the CME expands more strongly than it gains in height (Patsourakos et al. 2010a, 2010b; Cheng et al. 2013). Further, fast lateral CME expansion has been shown to be important for the formation of EUV waves and shocks low in the corona (e.g., Veronig et al. 2008; Temmer et al. 2009; Patsourakos et al. 2010a; Veronig et al. 2010; Cheng et al. 2012).

In this paper, we present a case study of the origin and early evolution of the fast CME that occurred together with the X8.2 flare on 2017 September 10 and its associated EUV wave. The event was the second-largest flare in solar cycle 24, and extreme in several aspects. It was associated with a very fast halo CME, with a speed $\gtrsim 3500 \text{ km s}^{-1}$ (Gopalswamy et al. 2018; Guo et al. 2018), and revealed distinct signatures of a long hot current sheet that formed behind the erupting structure (Seaton & Darnel 2018; Warren et al. 2018; Yan et al. 2018). The event produced widespread SEPs detected at Earth, Mars, and *STEREO-A*, i.e., covering a width of at least 230° in heliolongitude. Notably, this SEP event was the first ground-level enhancement (GLE) that was observed on the surface of two planets, Earth and Mars (Guo et al. 2018). *Fermi-LAT* observed an extremely long duration γ -ray event, detecting $>100 \text{ MeV}$ emission from the flare that lasted for more than 12 hr (Omodei et al. 2018). The associated EUV wave was also unique, as it was globally propagating across the full solar disk as observed from Earth view, as well as from *STEREO-A*, and showed transmission through both polar coronal holes (Liu et al. 2018; T. Podladchikova et al. 2018, in preparation). Some further aspects of this intriguing event that have been studied are the formation and turbulent plasma motions in the current sheet (Cheng et al. 2018; Li et al. 2018; Warren et al. 2018), the evolution of the flux rope, its cavity and reconnection

signatures (Long et al. 2018; Seaton & Darnel 2018; Yan et al. 2018), the coronal plasma properties in the aftermath of the CME (Goryaev et al. 2018), the microwave and hard X-ray flare emission (Gary et al. 2018), the shock properties near the Sun and the characteristics of the shock-accelerated particles (Gopalswamy et al. 2018), and the coronal-to-interplanetary CME evolution and associated wide shock (Guo et al. 2018).

We concentrate on the genesis, morphology, and impulsive dynamics of the CME in the low to mid-corona, as well as on its relation to the formation of the associated fast EUV wave. Very valuable observations on these phenomena are provided by the new Solar Ultraviolet Imager (SUVI; Seaton & Darnel 2018) on board *GOES-16*. SUVI observes the solar EUV corona over a large FOV, allowing us to robustly connect CME structures in subsequent images without change of instrument/emission processes, and with a cadence high enough to resolve the dynamical processes during the impulsive CME phase. These data are complemented by the high-cadence multiband EUV imagery of the Atmospheric Imaging Assembly (AIA; Lemen et al. 2012) on board the *SDO* (Pesnell et al. 2012), to study the impulsive evolution of the CME cavity and flux rope low in the corona. As we will demonstrate in this paper, the event under study provides us also with unique observations of the three-part CME structure from the EUV to the white-light coronagraph data and new insights into its physical interpretation.

2. Data

The SUVI instrument on board the *GOES-16* spacecraft images the solar corona in six EUV passbands, centered at 94, 131, 171, 195, 284, and 304 Å, with a large FOV, out to $>1.6R_s$ in the horizontal direction and as large as $2.3R_s$ in the unvignetted corners (Seaton & Darnel 2018), with R_s denoting the solar radius. The pixel scale of the SUVI filtergrams is $2''/5$. SUVI’s camera is equipped with an anti-blooming circuitry, which enables unobscured observations of the flare regions even in exposures where the detector is substantially saturated, while at the same time providing high sensitivity to observe faint structures (e.g., EUV waves). The AIA instrument on board *SDO* observes the solar EUV corona in seven wavelength bands, centered at 94, 131, 171, 193, 211, 335, and 304 Å, with a cadence as high as 12 s, a pixel scale of $0''/6$, and over an FOV of about $1.3R_s$ in the horizontal direction. Thus, AIA and SUVI both sample solar plasmas over a broad temperature range of about 10^5 – 10^7 K .

The X8.2 event of 2017 September 10 occurred when the source NOAA Active Region 12673 was on the western limb (flare start/peak time: 15:35/16:08 UT; heliographic coordinates: S08W88). SUVI and AIA observed the flare, the CME initiation and evolution in the low to mid-corona, and the associated EUV wave. We use the SUVI 195 Å filter observations available with a mean cadence of 1 minute to study the impulsive radial and lateral expansion of the CME shell, as well as the associated EUV wave. To enhance the structures in the images, in particular above the limb, we use the same filtering technique as in Seaton & Darnel (2018). This is a two-step filtering consisting of a varying radial filter (to account for the coronal intensity fall-off in the corona) and a temporal unsharp masking technique (to enhance changes in time). The image series was compensated for solar differential rotation, and base-difference images were created. In addition, we use the multiwavelength SUVI imagery to study the radial kinematics of the flux rope and cavity (Seaton & Darnel 2018).

Note that we did not rotate the SUVI images to north up, in order to keep the full FOV that SUVI provides; the solar P0 angle of the day was $+23^\circ.1$.

The SUVI data are complemented by the multitemperature EUV imagery from the AIA instrument on board *SDO*, to study the radial and lateral expansion of the distinct cavity observed low in the corona (Long et al. 2018). Each AIA image has been processed using the Multiscale Gaussian Normalization technique of Morgan & Druckmüller (2014) to highlight the fine structures above the limb. Data from the Large Angle and Spectrometric Coronagraph (LASCO; Brueckner et al. 1995) on board the *Solar and Heliospheric Observatory (SOHO)* are used to set the CME shell and cavity observed in the EUV into context with the white-light CME observed farther out by the LASCO C2 and C3 coronagraphs. The time line of the associated flare is studied in the *GOES* soft X-ray (SXR) and *Ramaty High Energy Solar Spectroscopic Imager (RHESSI)*; Lin et al. (2002) hard X-ray (HXR) data.

3. Results

3.1. Event Overview

Figure 1 and the accompanying movie give an overview of the early CME evolution and the formation of the EUV wave as observed in SUVI 195 Å direct images and corresponding base-difference images. In the movie, we can clearly see the expansion of the large preexisting loop system that develops into the CME shell, as well as the development of the associated EUV wave. We note that the pre-eruptive structure of the source AR 12673 is very distinct, consisting of a dense set of very large loops, with sizes up to $>0.5R_s$. These are a result of the extremely strong fields of >5000 G that have been measured in AR 12673 (Wang et al. 2018). In the movie, it is seen that the first motions and reconfigurations related to the event can be observed as early as 15:39 UT, including the rise of a low-lying, already-brightened prominence. During its rise, the prominence appears to dissolve and the eruption develops an inner flux rope structure with a clear cavity that is quickly expanding (see also Long et al. 2018; Seaton & Darnel 2018; Yan et al. 2018).

More detail of the CME formation and its early evolution can be seen in Figure 2 and the associated movie, which shows a zoom-in to the eruption region in six of the AIA EUV passbands. In the hot AIA 94 Å channel (dominated by emission from an Fe XVIII line; peak formation temperature $T \approx 7$ MK), the cavity is observed earliest, and also some embedded prominence material can be observed. The cavity becomes more pronounced during its fast rise and expansion. It appears dark in all AIA channels, indicative of a strong density depletion inside the cavity due to the enhanced magnetic pressure of the enclosed flux rope (e.g., Gibson 2015), and is surrounded by a distinct bright rim that can be seen in all AIA EUV passbands. Throughout the eruption, the bright rim is most distinct in the AIA 131 Å filter (Fe VIII and XXI), sampling plasmas at temperatures $\gtrsim 10$ MK. This suggests that the bright rim around the cavity may be a manifestation of the magnetic flux and frozen-in plasma that is fed to the erupting flux rope by the magnetic reconnection in the current sheet beneath, and that, hence, the hot cavity rim outlines the cross section of the enclosed expanding flux rope (as the simulations by Lin et al. 2004 suggest). This interpretation is further supported by the thin elongated structure that connects the

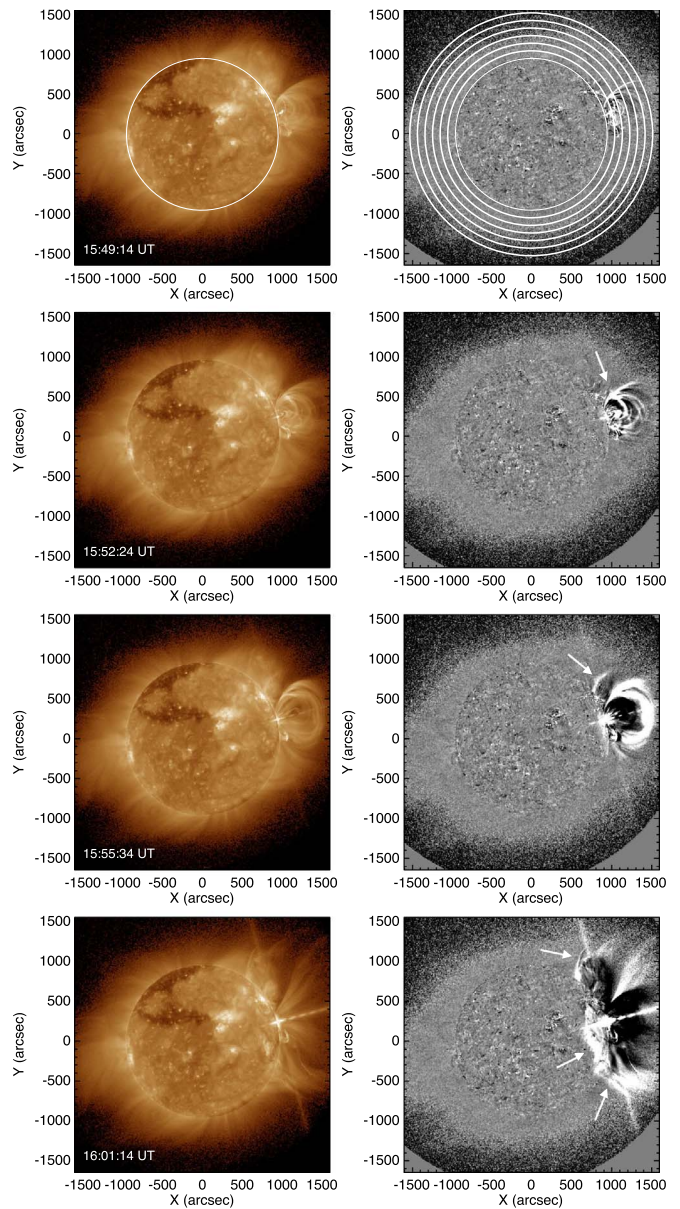


Figure 1. Overview of the 2017 September 10 event in SUVI 195 Å filtergrams. Left: direct images; right: base-difference images. In the first difference image, we overplot circles at heights of $(1.0\text{--}1.6)R_s$ in steps of $0.1R_s$, used to derive the stack plots shown in Figure 9. The arrows indicate the EUV wave observed above the limb and on the disk. The still figure shows the event at four time steps (annotated in each panel). The animated figure online shows the event evolution from 15:20:24 to 17:00:24 UT.

(An animation of this figure is available.)

bottom of the hot rim around the cavity to the top of the rising flare loop system, most clearly observed in the AIA 131 Å filter (see Figure 2 and associated movie). This structure has been interpreted as an observational signature of the hot plasma around the current sheet that is formed behind the eruption (Seaton & Darnel 2018; Warren et al. 2018; Yan et al. 2018). At later stages ($\gtrsim 16:00$ UT), after the cavity has already exited the AIA FOV, the elongated current sheet appears well pronounced in all the AIA EUV channels. As shown in Warren et al. (2018), the temperature in the current sheet is about 20 MK, with a relatively narrow distribution. The observed sheet thickness is about 3000 km (Yan et al. 2018).

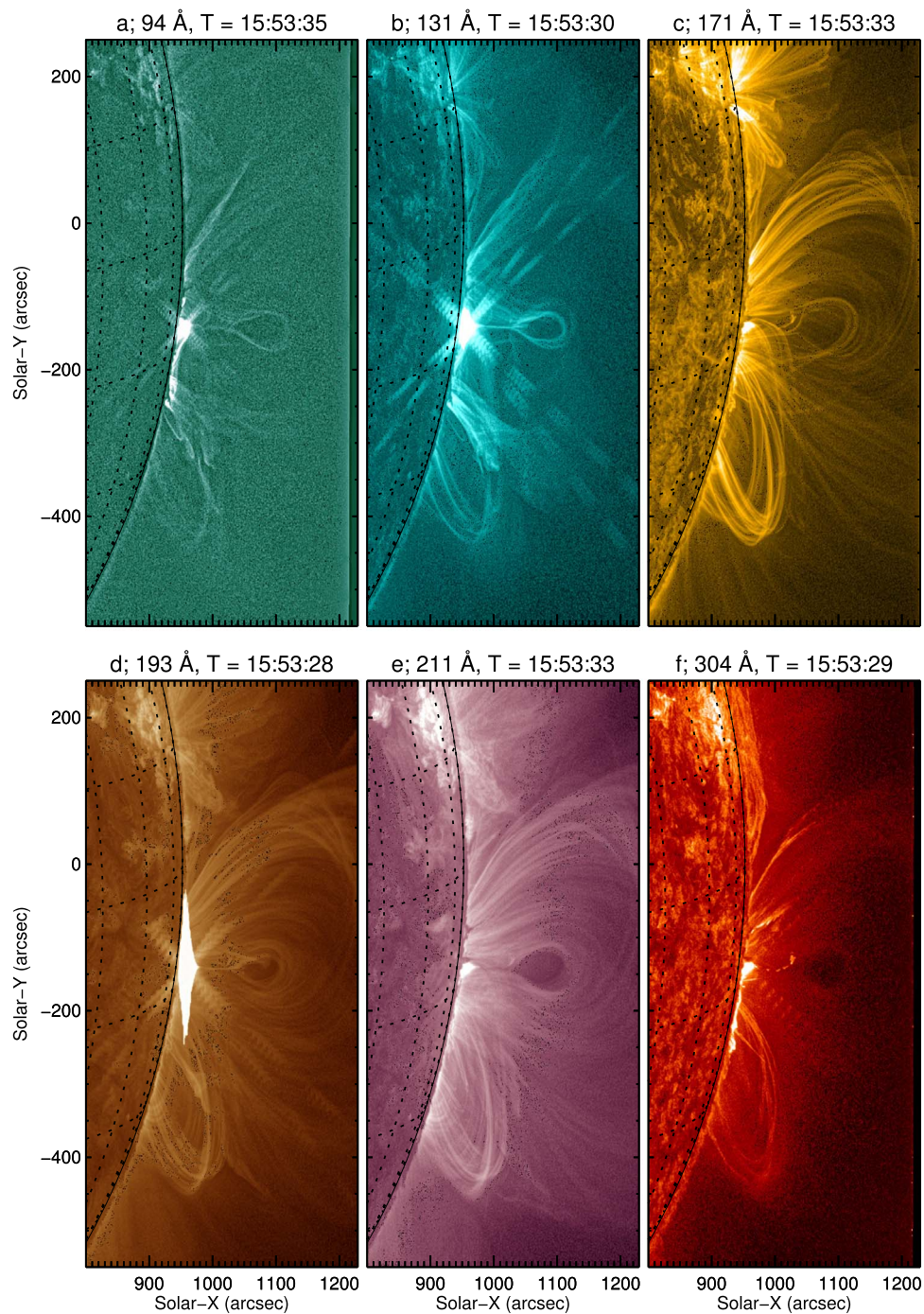


Figure 2. CME cavity as observed by *SDO/AIA* in the 94, 131, 171, 193, 211, and 304 Å filters. The still figure shows the cavity at one time step for each filter (annotated at each panel). The animated figure online shows the cavity evolution from about 15:17:30 to 16:40:00 UT.

(An animation of this figure is available.)

At the very start of the event, during 15:39–15:51 UT, hot loops are seen to reconnect and to form new configurations, as revealed in the AIA 131 and 94 Å images in Figure 2 and the associated movie. We can see changes in different flux systems connecting to the top of the flux rope structure. These changes are observed immediately before the cavity and bright rim are clearly formed and seem to be the trigger for the fast eruption.

The EUV wave associated with this event is distinctly seen above the solar limb as well as on the solar disk (Figure 1 and associated movie; see also Liu et al. 2018; Seaton & Darnel 2018). In the SUVI frame at 15:52:24 UT, we can identify the

wave for the first time, as it is formed ahead of the CME flanks expanding toward the north (indicated by an arrow in Figure 1). In this northern direction, the EUV wave appears as a sharp front above the limb growing to a large extension in height, up to the borders of the SUVI FOV. Toward the south, the formation and detachment of the wave from the CME flanks are not as distinct as toward the north, but after about 15:58 UT also here the EUV wave can be observed ahead of the CME shell in its propagation above the limb. On the disk, the EUV wave can be first identified in the SUVI frame at 15:54:24 UT. Surprisingly, despite the strength and global propagation of this

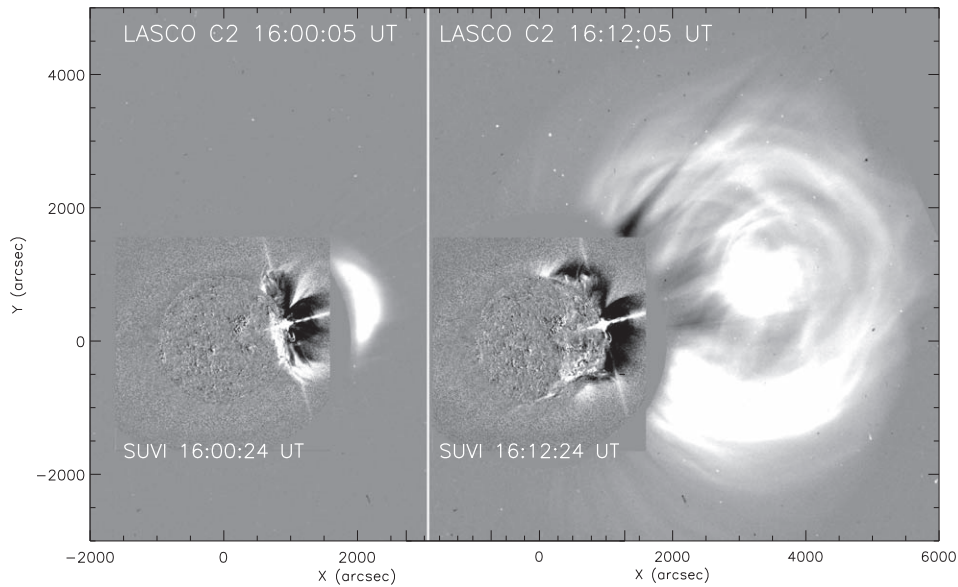


Figure 3. Composite SUVI 195 Å and LASCO C2 difference images, showing the connection of the CME outer front observed in the EUV to the white-light-coronagraph data. Note that the LASCO images are rotated to the SUVI orientation, i.e., to the P0 angle of $+23^\circ 1$.

EUV wave, inspection of the GONG $H\alpha$ image series did not reveal any signature of an associated Moreton wave.

The base-difference images in Figure 1 reveal a large coronal dimming above the limb, consisting of different parts signifying different magnetic domains and physical phenomena. The main dimming is associated with the CME eruption, as it is laterally well confined to within the expanding CME bubble. This is the coronal dimming due to the expansion and evacuation of mass by the erupting CME (e.g., Hudson et al. 1997; Zarro et al. 1999; Dissauer et al. 2018). The other dimming regions above the limb, farther apart from the eruption center in both the north and south directions, are more shallow and are trailing the propagating EUV wave front. These findings suggest that they are signatures of the rarefaction region that forms behind the compression front of the wave (Muhr et al. 2011; Lulić et al. 2013; Vršnak et al. 2016). The movie also reveals a number of interactions of the EUV wave with plasma structures in the corona, such as reflections, refractions, and, most interestingly, also the transmission through the polar coronal holes. These interactions and wave kinematics are studied in Liu et al. (2018) and Podladchikova et al. (2018, in preparation).

3.2. Early Dynamics of the Eruption

The event of 2017 September 10 provides us with an excellent opportunity to study the early impulsive dynamics of both the CME shell and the embedded flux rope/cavity in a very fast eruption. This is owed to the clearly formed and well-separated structures in this event captured by the high-cadence and large-FOV observations of the AIA and SUVI EUV imagers, respectively. Both phenomena are important to study, to better understand the origin of the eruption and its consequences. The flux rope represents a current-carrying structure that provides the forces driving the rise and expansion of the CME bubble. The dark EUV cavity that we observe is interpreted to map the flux rope’s cross section, as is further discussed in Section 3.2.2. The CME shell represents the outermost layer of compressed and piled-up material moving

through the corona and interplanetary space. It also acts as the contact surface that creates shock waves ahead of it.

Figure 1 and the associated movie show that following the early rise of the flux rope/cavity, the large preexisting set of loops observed in the SUVI 195 Å filtergrams also start to rise and to expand by successively piling up higher overlying sets of loops. It is also seen that the lateral expansion of this forming CME shell is more pronounced than the radial one, leading to a distinct lateral overexpansion. In Figure 3, we show composite images from the *SOHO*/LASCO C2 coronagraph and co-temporal SUVI 195 Å filtergrams for the first two time steps where the CME entered the C2 FOV. The composite at 16:00 UT clearly shows that the outer boundary of the loop structures that we see expanding in the SUVI 195 Å images seamlessly fits to the CME front observed in the white-light coronagraph data. In the northern direction, also some fainter outer emission region in C2 is seen, which appears to connect to the EUV wave front observed in SUVI that is already well separated from the CME shell at that time. This indicates that this faint outer emission region in C2 is an early signature of the CME shock wave observed in white light (see, Vourlidas et al. 2003). Finally, in the C2 image at 16:12 UT a bright core is seen, indicative of the embedded flux rope.

3.2.1. Early Dynamics of the CME Shell

In order to quantify the impulsive radial and lateral expansion of the CME shell in the SUVI FOV, we segment its structure and follow its evolution. At each time step, a binary map is constructed by thresholding, using the 2% brightest pixels in the SUVI 195 Å base-difference images. Figure 4(a) shows an example binary map derived, where all the white pixels are assumed to belong to the CME bubble. However, this segmentation includes also pixels without connection to the CME bubble, and these are subsequently removed by median filtering (Figure 4(b)). From this segmentation, we then determine the outer border of the CME structure and its (x,y) coordinates as shown by the red contour in Figure 4(c). Finally, missing parts of the border are determined by interpolation of the (x, y) coordinates on the

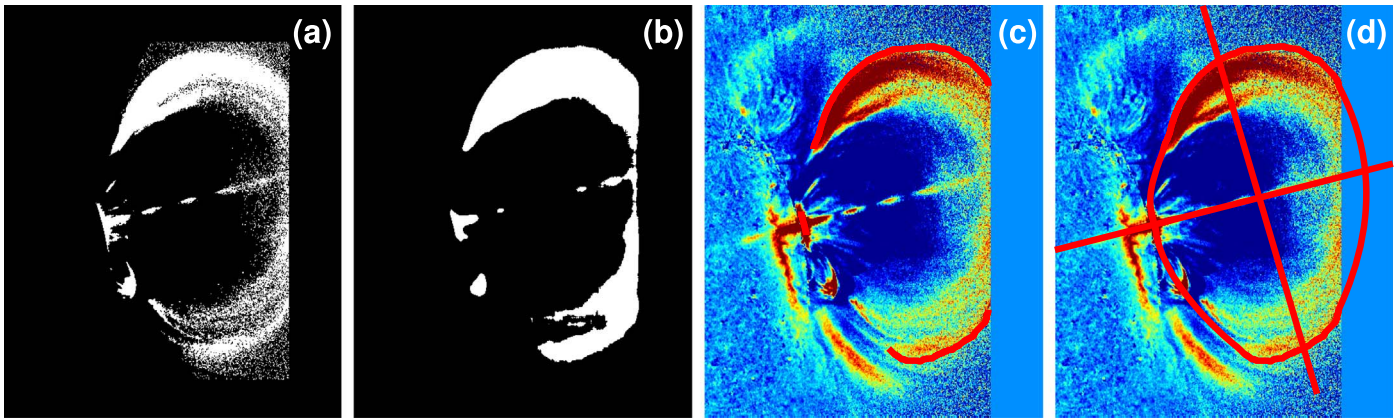


Figure 4. Illustration of the steps applied to segment the CME structure, shown for the SUVI 195 Å base-difference image at 15:57 UT. (a) Binary map derived by thresholding. (b) Segmented CME shell after median filtering. (c) Borders of the visible parts of the CME (red contour) on top of the SUVI base-difference image. (d) CME borders including the interpolated parts (red contour). The straight red lines indicate the radial and lateral directions through the center of the CME.

basis of minimization of the second derivative of the curve describing the border (Figure 4(d)). Note that with this approach we are able to automatically detect the outer envelope of the set of expanding EUV loops that is subsequently developing into the white-light CME (see Figure 3). Applying the segmentations on the SUVI base-difference images implies that we identify those regions that are increasing in emission owing to expansion and subsequent pileup of overlying loops, and thus becoming part of the overall erupting structure.

Figure 5 shows the results of this segmentation procedure for all SUVI 195 Å images during 15:49–15:57 UT. As can be seen from the determined borders, the shape of the CME structure transforms from roundish to an ellipse, indicative of a strong lateral overexpansion during its evolution. We also note that the segmentation algorithm correctly handles the loop system along the northern boundary, which is observed as a sharp, slightly curved radial structure. It exists already before the event, and the algorithm correctly identifies it as not being part of the CME shell. However, when the preexisting loop structure expands to form the CME, also the overlying loops are piled up and eventually become part of the CME shell. For the loop structure toward the north, this change is correctly identified between time steps 15:54 UT (where it is identified as an external structure, i.e., not part of the CME) and 15:55 UT (where it became integrated into the expanding CME shell).

Based on the CME segmentations at each time step, we trace its outward propagation along the radial direction from Sun center to the center of the CME structure. The height of the CME is then determined as its radial extent plus the distance between its lower border and the solar surface. The CME lateral expansion is analyzed by constructing the perpendicular line through the center of the segmented structure and determining the intersection points with its borders to determine the CME width (see the straight lines in Figure 5). The relative errors on the derived height and width data are estimated to be about 2%. These height and width measurements are then used to study the kinematics and dynamics of the CME shell. To obtain robust estimates of the corresponding velocity and acceleration profiles, we first smooth the height–time (width–time) curves and then derive the first and second time derivatives. The smoothing algorithm that we use for approximating the curves is based on the method described in Podladchikova et al. (2017), extended toward non-equidistant data. The algorithm optimizes between two (intrinsically conflicting) criteria in

order to find a balance between data fidelity, i.e., the closeness of the approximating curve to the data, and smoothness of the approximating curve. The data fidelity is evaluated by minimizing the sum of the squared deviations between the fit and the data points, and the smoothness is evaluated by minimizing the sum of squared second derivatives of the fit curve.

Figure 6 shows the evolution of the radial and lateral expansion of the CME. In panel (c), we plot the CME height (blue) and width (red) as a function of time. Panels (d) and (e) show the velocity and acceleration of the CME in radial (height) and lateral (width) direction. In addition to the smoothed curves, we also show the velocity and acceleration curves derived by numerical differentiation of the data points themselves. As one can see, the numerical derivatives, which are intrinsically very sensitive to noise, are in general well aligned with the smoothed curves. Due to the fast evolution, the changes over the mean observing cadence of 1 minute are big enough, so that in this case the noise on the direct derivatives is small. We also note that the slight “jump” in the CME lateral width evolution between 15:54 and 15:55 UT, which is due to the pileup of the loop structure observed to the northern boundary (as discussed above), is well handled by the smoothing algorithm applied on the kinematic curves (see Figure 6(c), red line). In panel (f), we plot the evolution of the CME aspect ratio r , defined as the height of the center of the CME shell above the solar limb divided by its half-width (see Patsourakos et al. 2010a, 2010b). The aspect ratio is basically a measure of the opening angle (angular width) of the CME, in the present case defined from its source region on the solar limb. In panel (f), we also plot the corresponding angular width of the CME derived as $W = 2 \arctan(1/r)$. In the top panels, we plot (a) the *GOES* 1–8 Å SXR flux and (b) the *RHESSI* HXR count rates in four energy bands from 12 to 300 keV, indicative of the evolution of the energy release and particle acceleration in the associated flare.

As can be seen from the kinematical curves in Figure 6, the CME reveals a very fast evolution. The radial propagation speed is continuously increasing and reaches $\sim 1000 \text{ km s}^{-1}$ at a distance of $0.85R_s$ above the limb. Later, in the coronagraphic FOV, the CME reached a maximum speed of $\gtrsim 3500 \text{ km s}^{-1}$ (Gopalswamy et al. 2018; Guo et al. 2018). The lateral CME expansion reveals a speed of $\sim 1600 \text{ km s}^{-1}$ in the SUVI FOV, reached within 4 minutes of impulsive acceleration. The

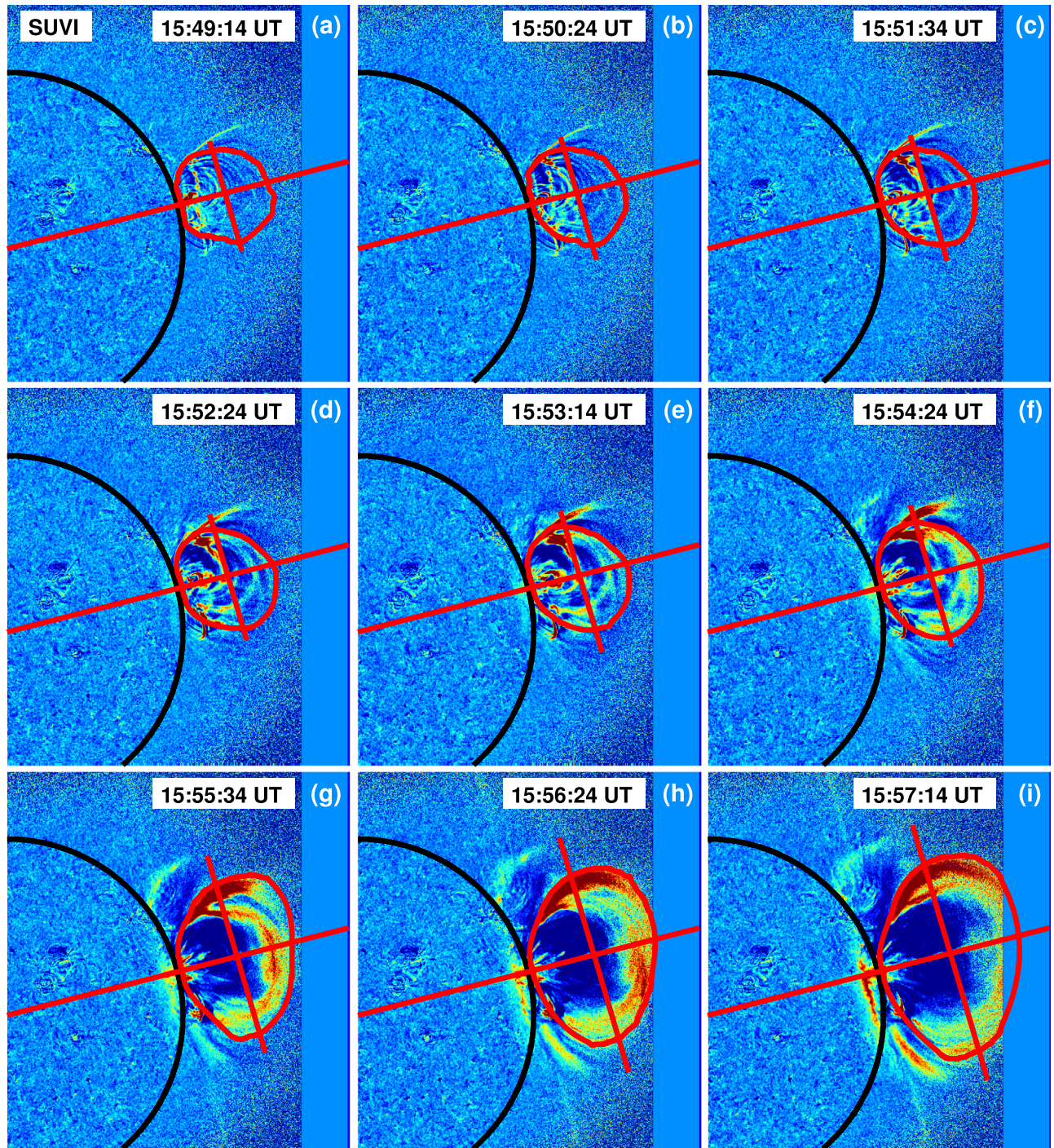


Figure 5. SUVI 195 Å base-difference images together with the outer borders of the segmented CME structure (red contours). The tracing of the CME radial and lateral expansion is indicated by the orthogonal straight red lines, respectively.

acceleration curves reach their maxima within the SUVI FOV, notably with much higher values for the lateral expansion, $10.1 \pm 1.1 \text{ km s}^{-2}$ at 15:53:50 UT, while the radial peak acceleration is $5.3 \pm 0.6 \text{ km s}^{-2}$ at 15:54:40 UT. The difference in the radial and lateral evolution causes a fast decrease of the CME aspect ratio, which changes from 0.96 to 0.75 within 5 minutes over a height range of just $0.2R_s$, corresponding to an increase of the CME angular width from about 90° to 105° . We note that the peaks in the lateral and radial CME acceleration occur simultaneously within the SUVI

measurement cadence of 1 minute, and also simultaneous with the first *RHESSI* 100–300 keV HXR burst (15:54:40 UT).

3.2.2. Cavity Morphology and Flux Rope

As discussed in Section 3.1, the cavity embedded inside the CME shell appears dark in all AIA EUV channels, suggestive of a strong density depletion due to the enhanced magnetic pressure in the enclosed magnetic flux rope, and it is surrounded by a bright rim (see Figure 2). Throughout the eruption observed in the AIA FOV, this rim appears most

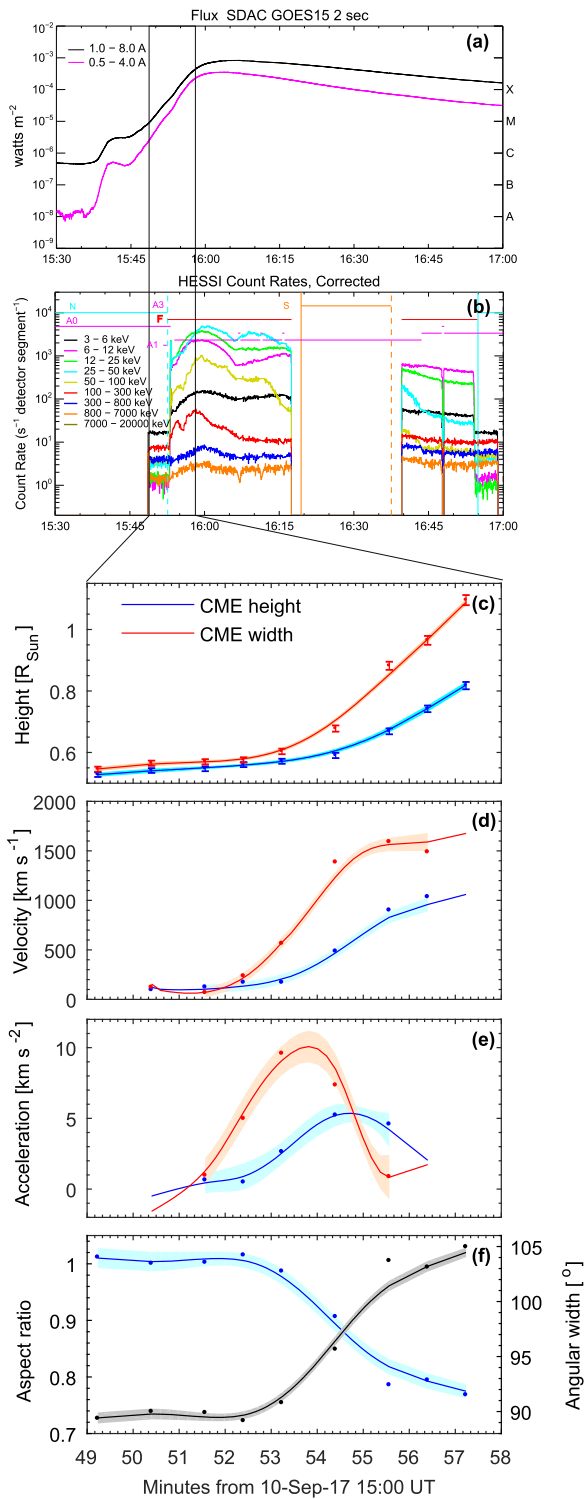


Figure 6. Impulsive phase of the radial and lateral evolution of the CME shell, and associated flare emissions. (a) Flare emission recorded in the *GOES* 0.5–4 and 1–8 Å SXR bands. (b) *RHESSI* hard X-ray count rates in four energy bands from 12 to 300 keV. (c) CME height (blue circles) and CME width (red circles) determined from *SUVI* 195 Å images (see Figure 5) together with error bars. The corresponding lines show the smoothed height–time and width–time profiles. (d) Velocity and (e) acceleration of the CME radial (red) and lateral (blue) expansion obtained by numerical differentiation of the data points (circles) and the smoothed curves (lines). The shaded regions outline the error ranges obtained from the smoothed curves. (f) CME aspect ratio (blue) and angular width (black).

pronounced in the 131 Å filter, together with the hot current sheet ($T \approx 20$ MK; Warren et al. 2018) beneath which the hot cavity rim connects to the top of the rising flare loop system. The high plasma temperatures in the bright rim around the expanding cavity are confirmed by the AIA differential emission measure (DEM) analysis in Yan et al. (2018) and from *Hinode*/EIS spectroscopy, which shows the rim around the expanding cavity most prominently in the Fe XXIV spectral line (see Figure 4 in Long et al. 2018), sampling plasmas at temperatures of about 15 MK. Note that the DEM maps shown in Yan et al. (2018, Figure 4 therein) suggest that the thin cavity plasma embedded *inside* the bright hot rim is also hot.

It is important to note that a bright rim around the cavity is observed in all AIA channels, i.e., those sampling hot plasma at about 10 MK (131, 94 Å), as well as the “cooler” filters, which are most sensitive to plasma at typical quiet coronal temperatures in the range 1–2 MK (171, 193, 211 Å). However, there are also differences in the cavity/rim morphology as observed in the hot and cooler filters, which have important implications. In particular, we note that the bright rim and enclosed cavity have different sizes in the different AIA filters, appearing smallest in the hot AIA passbands. This size difference is clearly seen in the co-temporal AIA 131 and 211 Å snapshots plotted in Figure 7, where the hot bright rim observed in AIA 131 Å well fits inside the dark cavity observed in the AIA 211 Å filter.

The smaller hot rim around the cavity, as most distinctly observed in the 131 Å filter, is strongly suggestive of additional magnetic flux that is supplied to the flux rope by magnetic reconnection in the current sheet beneath. Since the plasma contained in this flux is heated by the reconnection as it passes through the current sheet, it does not contribute to the emission in the EUV channels sensitive to lower temperatures, so that these passbands show the whole cross section of the flux rope as a dark cavity. These observations provide strong evidence that the distinct EUV cavity and surrounding hot rim observed in this event outline the cross section of the expanding flux rope, including the layer of newly added flux by magnetic reconnection in the current sheet.

The bright rim observed in cooler plasmas like in 211 Å, which has its inner boundary located at the outer boundary of the hot rim observed in 131 Å (red ellipses in Figure 7; see also the movie associated with Figure 2), is most likely formed by the compression of the plasma in the nearby overlying loops that get piled up by the rising and expanding flux rope. This is before the corresponding field lines also come to magnetic reconnection in the current sheet beneath, and a hot rim is formed around the cavity where a cool rim was observed before.

3.2.3. Early Dynamics of the Flux Rope/Cavity

In the following, we study the dynamics of the flux rope/cavity by measuring its radial and lateral expansion and outward motion. We use the measurements of Long et al. (2018), who manually identified the inner edge of the bright rim around the cavity separately for four different AIA passbands, and then fitted these contours by an ellipse, extracting its minor and major axes, as well as the height of its center above the limb (see Figure 2 therein). Here we use the width (minor axis) and height of the cavity center derived from

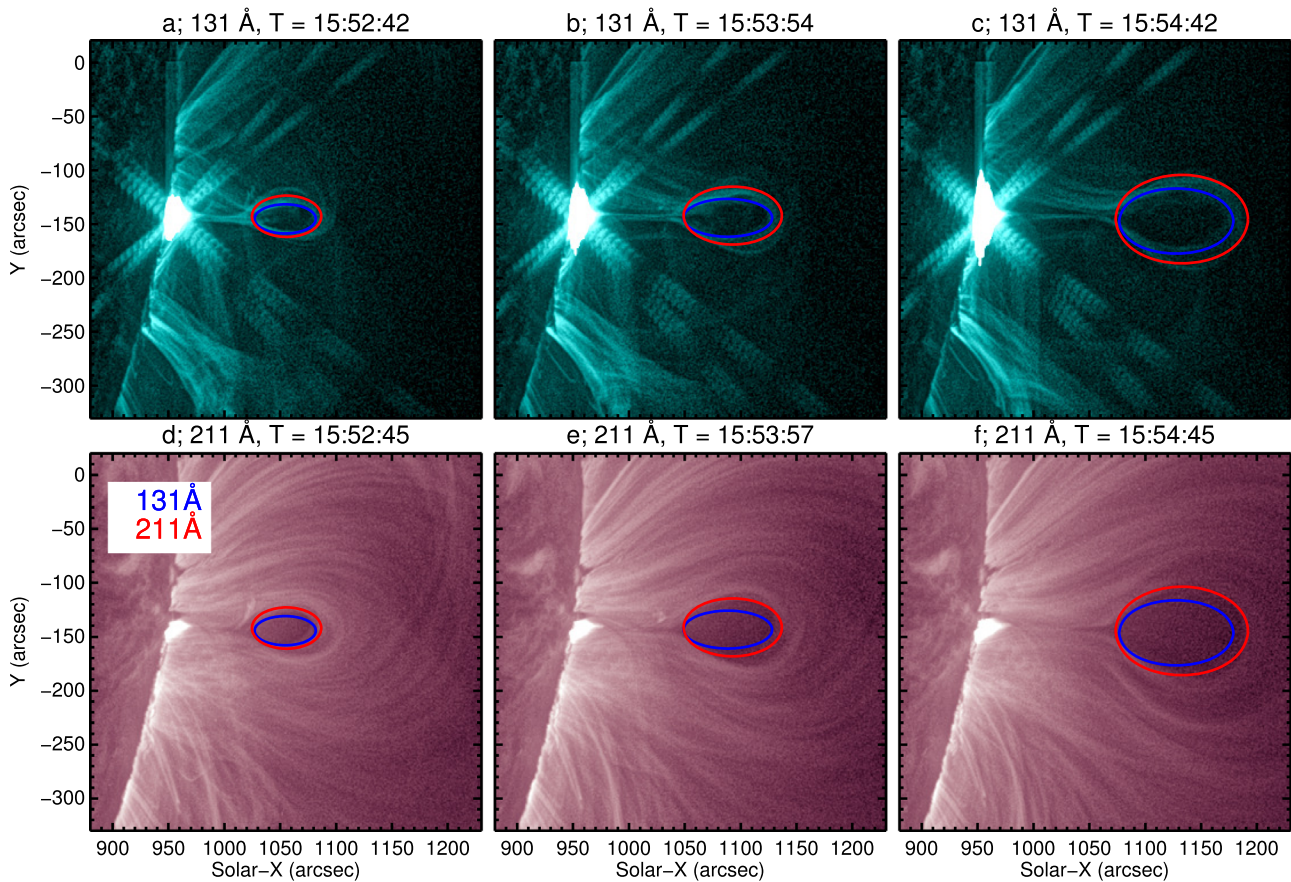


Figure 7. Snapshots of the eruption observed in the AIA 131 Å (top) and 211 Å (bottom) filters. The blue (red) contours outline the ellipses fitted to the inner edge of the bright rim around the dark cavity as observed in AIA 131 (211) Å. The ellipse fits are from Long et al. (2018).

the AIA 211 Å images, as they contain the most complete set of measurements. Note that these measurements of the kinematics of the dark cavity observed in AIA 211 Å (inner edge) basically correspond to the outer boundary of the bright rim in AIA 131 Å (see Figure 7 and Section 3.2.2). In addition, we use the measurements of Seaton & Darnel (2018), who visually tracked the center of the rising flux rope and cavity combining all SUVI filters to derive its height evolution (see Figure 2 therein). The additional value of the SUVI data is that we can follow the flux rope across a larger height range than in AIA and thus measure its full impulsive acceleration phase.

In Figure 8, we show the results for the kinematics and dynamics of the CME cavity/flux rope, using the same methods as for the analysis of the CME shell described in Section 3.2.1. We plot (a) the height of the center of the flux rope/cavity and its width, (b) the derived velocity and (c) acceleration profiles of the cavity height and width, as well as (d) its aspect ratio and angular width. As can be seen in panel (a), the measurements of the cavity/flux rope height from Long et al. (2018) and Seaton & Darnel (2018) are in agreement with each other despite being derived from different instruments and with different methods. The radial propagation of the cavity/flux rope starts with a slow rise phase (first measurements of Seaton & Darnel 2018 are from 15:44 UT), changing to a faster increase around 15:51 UT. At 15:57:30 UT at a distance of $0.5R_s$ above the limb (when it exits the SUVI FOV), it reaches $\sim 1600 \text{ km s}^{-1}$, and the speed is still increasing. The width of the cavity first reveals a slow continuous expansion, which then quickly increases at 15:53 UT, reaching an expansion speed of

$\sim 500 \text{ km s}^{-1}$ about 2 minutes later when it exits the AIA FOV; the corresponding speed of its radial motion at this time is $\sim 800 \text{ km s}^{-1}$.

The acceleration of the lateral expansion (cavity width) reveals a maximum of $5.3 \pm 1.1 \text{ km s}^{-2}$ at 15:53:40 UT, while the acceleration of the radial motion of its center reaches a peak of $6.7 \pm 0.9 \text{ km s}^{-2}$ at 15:55:20 UT. Notably, the radial acceleration reveals a more continuous profile, constantly increasing over about 6 minutes until reaching its maximum, whereas the acceleration profile of the cavity width is more impulsive with a full duration of less than 3 minutes. The aspect ratio (angular width) reveals a slow increase (decrease) in the early phase followed by a fast decrease (increase) starting at 15:53:20 UT, during which the angular width of the cavity increases from 18° to 28° over just 2 minutes, indicative of a strong lateral overexpansion of the cavity during this phase.

3.3. Associated EUV Wave

In order to study the formation of the associated EUV wave and its relation to the expanding CME shell, we show in Figure 9 stack plots generated from SUVI 195 Å base-difference images along circular slits at various distances from Sun center, corresponding to heights of $r = (0.05-0.6)R_s$ above the solar surface (see Figure 1, top right panel). The emission is averaged over a thin circular layer covering the width of 2 SUVI pixels (corresponding to 5 arcsec) across the considered radial distance, and then we stacked the slits obtained at different time steps. Each stack plot in Figure 9 shows, for a certain radial distance r from Sun center, the emission

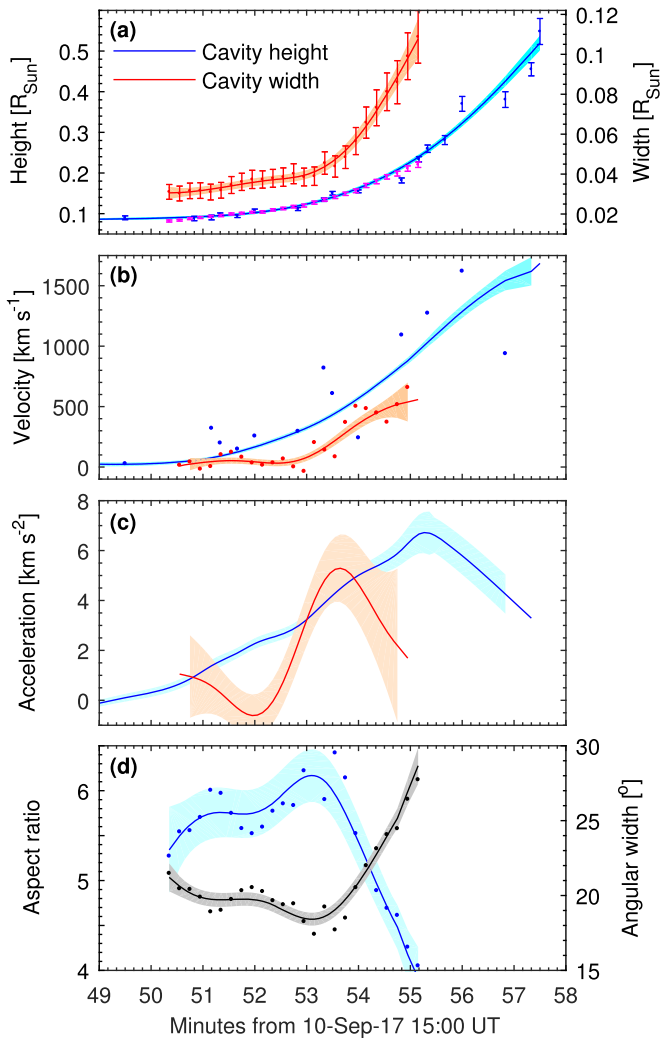


Figure 8. Evolution of the CME cavity. (a) Height and width of the CME cavity, together with error bars. The corresponding lines show the smoothed height–time and width–time profiles. Height is determined from multi-wavelength SUVI data (blue; measurements from Seaton & Darnel 2018) and AIA 211 Å images (pink; measurements from Long et al. 2018). Width is determined from AIA 211 Å images (red; measurements from Long et al. 2018). (b) Velocity and (c) acceleration of the radial (red) and lateral (blue) expansion of the cavity obtained by numerical differentiation of the data points (circles) and the smoothed curves (lines). The shaded regions outline the error ranges obtained from the smoothed curves. (d) Aspect ratio (blue) and angular width (black) of the cavity (derived from measurements in Long et al. (2018).

enhancement with respect to a pre-event base image as a function of the polar angle φ (on the y -axis) and time (x -axis). The counting of φ starts at the left (eastern) horizontal line of the SUVI images, and the eruption center is located at $\varphi = 166^\circ$ (indicated by the cyan line in Figure 9).

The stack plots shown in Figure 9 clearly show the impulsive lateral expansion of the CME flanks, the EUV wave that is formed and propagating ahead of the CME flanks, and the coronal dimmings behind. There is an obvious asymmetry in the behavior toward the northern and southern directions. Toward the north, the EUV wave front is clearly detached from the expanding CME flank and propagating ahead of it. The EUV wave is formed as early as 15:52:24 UT at heights $\lesssim 0.2R_s$ above the solar limb. This is 1.5 minutes before the peak of the acceleration of the lateral expansion of the CME shell, but at that time the lateral acceleration is already as high as 6 km s^{-2}

(see Figure 6). Note that this formation time of the EUV wave also well coincides with the start of the strong decrease in the aspect ratio of the CME shell, i.e., the strong lateral overexpansion. At the time of first EUV wave detection (15:52:24 UT), the distance of the wave front is only 38 Mm ahead of the contact surface, i.e., the lateral outer boundary of the CME shell. During its evolution, the distance of the wave front from the CME flanks quickly increases and the wave front grows in height, reaching up to the edge of the SUVI FOV. In the stack plots in Figure 9, the track of the propagating wave front can be clearly identified and measured up to heights of at least $0.5R_s$ above the limb. The behavior in the southern direction is quite different. Here, it is only at times $\gtrsim 15:58$ UT that the EUV wave can be distinguished from the CME structure, and it is observed only at lower heights, up to about $0.3R_s$.

In Figure 9, we have also indicated the outer fronts of the CME flank (blue lines) and the EUV wave (black lines), the latter being used to estimate the mean speed of the EUV front at different heights above the limb. The results reveal an increase of the EUV wave speed with height, in the northern direction from 750 km s^{-1} at $0.05R_s$ to 1200 km s^{-1} at $0.5R_s$, with the strongest increase taking place between $0.4R_s$ and $0.5R_s$ above the solar limb. In the southern direction, we also observe a height dependence of the EUV wave speed, increasing from 750 to 950 km s^{-1} from $0.05R_s$ to $0.3R_s$.

4. Discussion and Summary

The X8.2 flare/CME event of 2017 September 10 provides us with a unique opportunity to study the origin, morphology, and impulsive dynamics of a very fast eruption ($v \gtrsim 3500 \text{ km s}^{-1}$), as well as its relation to the fast EUV wave formed. In the present case we can observe and measure both the evolution of the outer CME shell and the embedded flux rope/cavity. This is thanks to the combination of the high-cadence EUV imagery of SUVI and AIA, covering the low and middle corona, where the impulsive CME dynamics takes place. In addition, this unprecedented set of observations reveals important implications for the three-part structure of CMEs.

4.1. Impulsive Dynamics of the CME Shell and Cavity/Flux Rope

The early evolution of the CME shell is well observed in the SUVI 195 Å filtergrams. It develops from a set of very large preexisting loops (with sizes up to $>0.5R_s$). During their expansion, successively higher overlying loops are piled up and become part of the erupting structure (see Figure 1 and associated movie, as well as Figure 5). Comparison with the images by the LASCO C2 coronagraph shows that the outer front of these expanding and piled-up loops observed in the EUV images seamlessly matches with the CME front observed in white-light coronagraph images (Figure 3).

The event also reveals a distinct cavity embedded in the CME shell, strongly indicative of the flux rope. Magnetic reconfigurations indicative of reconnection are observed early in the event (most prominently in the AIA 131 Å passband), connecting the forming flux rope structure to the northern and southern footpoints of the large-scale overlying loops observed in SUVI 195 Å images. These reconnections appear to trigger the eruption, during which the cavity becomes well pronounced

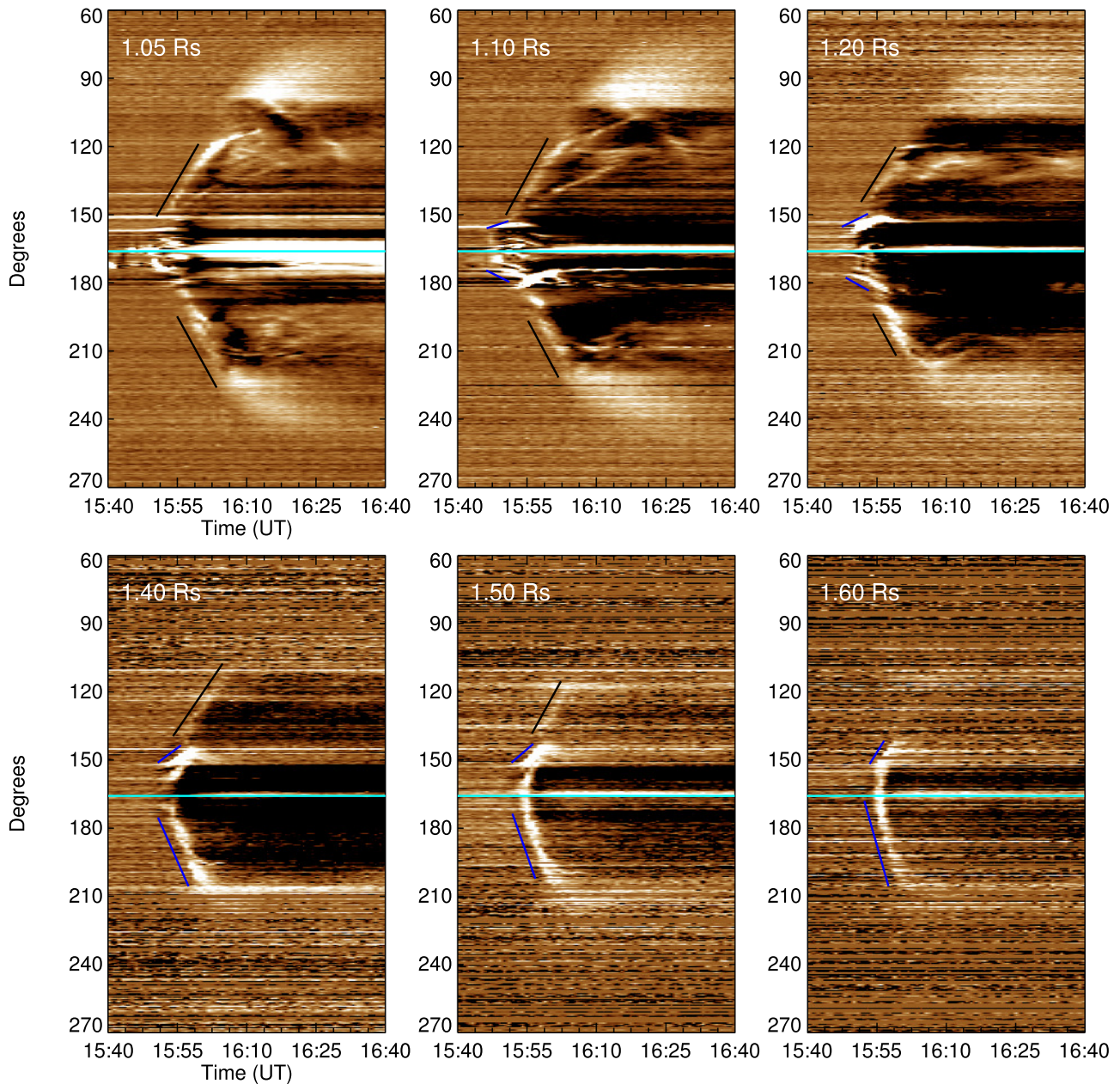


Figure 9. Stack plots derived from SUVI base-difference images in circular slits with increasing radius, ranging from $1.05R_s$ to $1.6R_s$ (see Figure 1) from Sun center. The horizontal line marks the center of the eruption. The CME flanks and the EUV wave fronts are marked by blue and black lines, respectively. To keep the visibility of the tracks in the stack plots, the lines are shifted toward the left (by 2 minutes).

and is quickly expanding and rising (see Figure 2 and accompanying movie).

The expanding cavity appears dark in all AIA channels, indicative of the density depletion inside the cavity due to the enhanced magnetic pressure of the enclosed flux rope (e.g., Gibson 2015), and it is surrounded by a bright rim. The hot bright rim (most distinctly observed in AIA 131 Å filtergrams) that develops around the expanding dark cavity has temperatures in the range $T \approx 10\text{--}15$ MK (Long et al. 2018; Yan et al. 2018), and its lower boundary is connected to the rising cusp-shaped flare loop system by a hot ($T \approx 20$ MK) and thin elongated current sheet (Yan et al. 2018; Warren et al. 2018). In the cooler coronal AIA 171 Å filter, reconnection inflows into the current sheet were observed with velocities of about 100 km s^{-1} (Yan et al. 2018). All these findings strongly

suggest that the hot rim around the expanding cavity is a manifestation of the new flux and heated plasma that is added to the flux rope by magnetic reconnection in the current sheet beneath.

The role of reconnection for the CME dynamics lies in transferring magnetic flux from the ambient field into poloidal flux of the flux rope, which is associated with the current in the flux rope. This additional flux is important for the CME acceleration, as it strengthens the hoop force acting on toroidal flux ropes (Shafranov 1966; Chen 1989) and reduces the effect of the inductive decay of the electric current in the expanding flux rope (Vršnak 2008, 2016). The reconnected flux typically changes with time from a considerably sheared to a nearly purely poloidal one, as indicated by the well-known evolution of the flare loops in many events (e.g., review by Fletcher et al. 2011).

The ratio of toroidal and poloidal flux also differs from event to event. In the present case, the formation of a complete rim around the erupting flux rope indicates that the reconnected flux is dominantly poloidal from the beginning of the event (also see Section 4.3).

In the 2017 September 10 event, the CME shell and the cavity reveal an unprecedented fast evolution. The peak accelerations of both the lateral and radial expansion of the segmented CME shell are reached within the SUVI FOV. The lateral CME expansion reaches a peak acceleration of $10.1 \pm 1.1 \text{ km s}^{-2}$, and in the radial direction we find a peak of $5.3 \pm 1.4 \text{ km s}^{-2}$ at a height of $0.62R_s$ above the limb. Such high lateral acceleration values have not been reported before, and the radial acceleration also is among the highest values reported. Statistically, CME peak accelerations lie mostly in the range of $0.1\text{--}1 \text{ km s}^{-2}$ (Zhang & Dere 2006; Vrřnak et al. 2007; Bein et al. 2011; Břak-Steřlicka et al. 2013). To our knowledge, only six CMEs have been reported with peak radial accelerations of the CME front $\gtrsim 5 \text{ km s}^{-2}$ (Zhang et al. 2001; Williams et al. 2005; Vrřnak et al. 2007; Temmer et al. 2008; Bein et al. 2011; Ying et al. 2018). Lateral accelerations of the CME flanks are rarely derived, owing to the difficulties in extracting the whole CME structure low in the corona. The highest values we found in the literature are in the range of $1\text{--}2 \text{ km s}^{-2}$ (Patsourakos et al. 2010a, 2010b; Cheng et al. 2012).

We note that in a very recent paper on this event by Gopalswamy et al. (2018), a peak value of the radial CME acceleration of $9.1 \pm 1.6 \text{ km s}^{-2}$ at 15:58 UT at a height of $2.05R_s$ from Sun center is claimed. However, looking into their kinematics plot (Figure 2 therein), it is clear that this value is an artifact, arising from the transition between two instruments when changing the measurement data from EUVI to COR1, which results in a local jump of the distance–time curve. There is never a perfect transition in such combined measurements, because of different emission mechanisms and sensitivities of different instruments. Thus, careful smoothing would be needed to properly account for such discontinuities. However, in Gopalswamy et al. (2018) the velocity and acceleration profiles are derived from direct numerical differentiation of the height–time measurement points. As one can see from their Figure 2, the reported high (second) peak in the CME acceleration is obtained exactly at the time where the measurements change from EUVI to COR1, and is a mere artifact of the numerics when calculating the first and second time derivatives without accounting for instrumental discontinuities and noise in the data.

The acceleration of the width of the cavity occurs synchronized with the width of the CME shell. They reach their peak acceleration at 15:53:40 and 15:53:50 UT, respectively, with values of $5.3 \pm 1.4 \text{ km s}^{-2}$ (cavity) and $10.1 \pm 1.1 \text{ km s}^{-2}$ (CME shell). The peak accelerations of their radial outward motion appear slightly later but again roughly synchronized, with a value of $6.7 \pm 0.6 \text{ km s}^{-2}$ reached at 15:55:20 UT for the CME cavity and with a value of $5.3 \pm 0.6 \text{ km s}^{-2}$ at 15:54:40 UT for the CME shell. These peak times of the radial accelerations are also close in time to the peak of the first *RHESSI* 100–300 keV HXR burst (15:54:40 UT) of the associated flare, further underlining the importance of the reconnection process for the CME impulsive evolution. The magnetic reconnection in the current sheet that is formed below the erupting flux rope provides for the energy release of the flare, as well as additional magnetic flux to the flux rope to further facilitate its acceleration. This

coupling and feedback relation establishes a synchronization of both processes, i.e., the flare energy release, associated particle acceleration, and the CME dynamics (Neupert et al. 2001; Zhang et al. 2001; Vrřnak et al. 2004; Temmer et al. 2010; Berkebile-Stoiser et al. 2012).

Here, we demonstrate for the first time that the distinct hot rim observed around the flux rope cavity is a manifestation of the dominantly poloidal flux and frozen-in plasma that is subsequently added to the expanding and rising flux rope by reconnection in the strong event under study. An implication of these unique observations is that, due to the very strong fields of up to 5 kG (Wang et al. 2018) and the large system of densely packed loops in the source NOAA AR 12673, as observed in the EUV images, the values for the magnetic flux and plasma densities of the reconnected loops are very high. These findings also explain why, in this event, the (lateral and radial) accelerations in the flux rope and CME shell reach such extremely high values; all peak values lie in the range of $5\text{--}10 \text{ km s}^{-2}$. Vrřnak (2016) modeled a curved flux rope anchored in the photosphere, being subject to the kink and torus instability. He found that in the most strongly accelerated eruptions, in which peak values of the order of 10 km s^{-2} are reached, the poloidal flux supplied by magnetic reconnection has to be several times larger than the initial flux in the pre-erupting flux rope.

4.2. Overexpansion and Relation between CME Shell and Cavity Evolution

The CME shell and the cavity reveal not only an unprecedented fast evolution, but also a very strong overexpansion in the low to mid-corona, i.e., the sizes (widths) of the structures expand much faster than they gain in height (see Patsourakos et al. 2010a, 2010b). Farther out in the coronagraphic FOV, generally an approximate self-similar CME evolution is observed, i.e., the CME size and height increase at the same rate (Schwenn et al. 2005), keeping the angular width and aspect ratio approximately constant. For the early evolution of the CME shell, we find an impulsive decrease of the aspect ratio from 0.98 to 0.75 during 15:53 to 15:57 UT, corresponding to an increase of its angular width (measured from its source region on the limb) from about 90° to 105° . Guo et al. (2018) derived an angular width of about 130° from graduated cylindrical shell (GCS) fitting of the CME observed by the coronagraphs on board *LASCO* and *STEREO-A*. This indicates that the CME width was still increasing after it left the SUVI FOV, which is consistent with the still-increasing evolution seen in Figure 6(f). For the cavity, we find first (from 15:50 to 15:53 UT) a slight decrease of the angular widths, before changing to an impulsive increase during 15:53–15:55 UT (when it exits the AIA FOV) from 18° to 28° (Figure 2(d)).

It is important to note that, in the lateral direction, the CME shell expands much faster than the cavity (compare the red curves in Figures 6(d) and 8(b)). This is also true for the loops *between* the cavity (flux rope) and the CME shell (see the 171, 193, and 211 Å channels in the animation of Figure 2). This means that, at these heights, these structures are not piled up by the expanding flux rope, but rather move away from it. More specifically, the CME shell is piled up by the expanding motion of ambient coronal loops in the intermediate environment of the flux rope (in a distance range comparable to the height of the flux rope) as the loops move away from the flux rope and press against the more distant coronal environment. This process

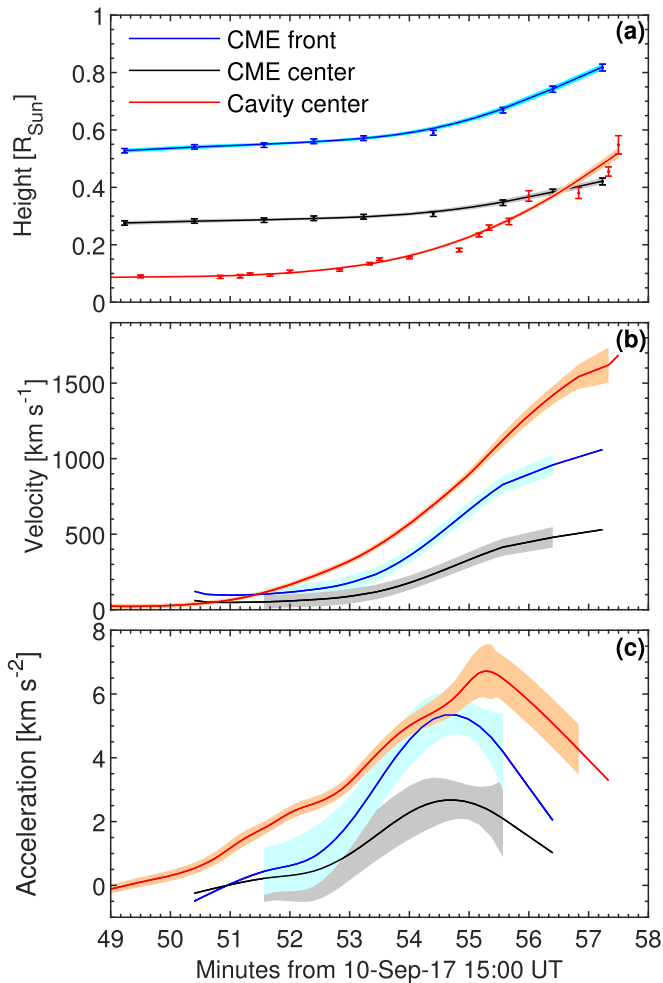


Figure 10. Combined radial evolution of CME shell and cavity. (a) Height of the outer front of the CME shell (blue circles), the center of the CME shell (black circles), and the center of the cavity (red circles), together with error bars. The corresponding lines show the smoothed height–time profiles. (b) Corresponding velocity and (c) acceleration profiles, with the shaded regions outlining the error ranges obtained from the smoothed curves.

obviously is part of the genesis of the CME, as it contributes to the formation of the CME shell and its enclosed cavity in the early stages of the eruption (roughly within $1R_s$ above the photosphere). The expanding motion of ambient flux, away from the rising flux rope, has been noted by Patsourakos et al. (2010a), who suggested that it is a consequence of decreasing current through the flux rope as it rises. Kliem et al. (2014) termed this a “reverse pinch effect” and confirmed it in MHD simulations of erupting flux ropes (full manuscript in preparation).

In the radial direction, the situation is reversed: here the cavity (flux rope) rises faster than the overlying loops and CME shell (blue curves in Figures 6(d) and 8(b)). This speed difference in the radial direction is seen more clearly in Figure 10, where we jointly plot the kinematics of the outer front of the CME shell, the center of the CME shell, and the center of the cavity. It is clearly seen how the cavity moves forward inside the CME shell (panel (a)) from close to its bottom to beyond its center, owing to its much higher velocity (panel (b)). Since the reverse pinch effect should operate in the vertical direction in the same way as in the lateral direction, the different behavior, which results in the lateral overexpansion of the CME shell, can only be explained by a stronger restraining

force of the ambient corona in the vertical direction. The preexisting set of prominent large-scale coronal loops that pass over the eruption site at about $0.5R_s$ may provide this through a primarily downward-directed tension force. High-reaching overlying loops typically run nearly perpendicularly to the polarity inversion line, so that they resist the upward expansion of an erupting flux rope more than the lateral expansion, especially the lateral expansion perpendicular to the loops. Additionally, the perturbation of a dominantly gravitationally stratified ambient corona by a developing CME can lead to a preferentially downward-restraining force and lateral overexpansion of the CME (Pagano et al. 2013). However, the plasma beta in an active region with very strong photospheric field strengths (up to 3 times higher than those assumed in Gary 2001) at heights of $\sim 0.5R_s$ is still much smaller than unity, so that in the present event the pressure gradient force of the ambient corona is less likely to cause the overexpansion than the strong overlying loops.

4.3. Implications for the CME Three-part Structure

The distinct observations of the 2017 September 10 eruption provide us with important insight into the magnetic morphology of the erupting structure. We observe a hot bright rim around a quickly expanding dark cavity, which is embedded inside a much larger CME shell. The CME shell develops from a dense set of large preexisting AR loops (with sizes up to $>0.5R_s$). During their expansion, successively higher overlying loops are piled up and become part of the overall erupting structure (see Figures 1 and 5). The CME shell is best observed in the cooler filters of the SUVI and AIA instruments (171, 195, 211 Å) sampling plasma at quiet coronal temperatures around 1–2 MK. The hot rim around the expanding cavity is most distinctly observed in the AIA 131 Å filter and has plasma temperatures in the range of 10–15 MK (Long et al. 2018; Yan et al. 2018). It is a manifestation of the flux and frozen-in plasma that is added to the rising flux rope by magnetic reconnection in the current sheet beneath. As the plasma trapped on the coronal loops overlying the erupting structure is brought into the current sheet below by the reconnection inflow, it gets heated by the magnetic reconnection process. The heated plasma frozen to the downward-closing flux builds up the hot flare loop system, whereas the heated plasma frozen to the upward ejected poloidal fields forms the expanding hot rim around the flux rope.

The event under study also shows exceptionally well that the lower boundary of the hot rim around the cavity is connected to the rising flare loop system by a large-scale thin vertical current sheet, almost perfectly like in the eruptive flare cartoon in Figure 1 in Lin et al. (2004). Gary et al. (2018) report sources of nonthermal microwave and hard X-ray emission indicative of accelerated electrons above the hot cusp-shaped flare loops, with the microwave sources extending even higher up into the indicated current sheet region. The thermal plasma in the elongated current sheet has been diagnosed to have temperatures of about 20 MK (Warren et al. 2018). These observational findings also provide strong evidence that in the present case the dark cavity outlines the cross section of the flux rope, which is quickly expanding owing to the continuously added flux by the magnetic reconnection in the current sheet behind the erupting structure. We note that the formation of a bright rim around quickly expanding flux ropes due to the reconnected poloidal flux and plasma has been derived in the framework of

the loss-of-equilibrium model (Lin et al. 2004). However, to our knowledge, this is the first event showing it in observational data in perfect agreement with the theoretical prediction.

What are the reasons that, in the event under study, all these structures are so well observed? In addition to the obviously favorable geometry with respect to the line of sight (i.e., that we look along the axis of the rising flux rope) and the excellent observational coverage of the low to mid-corona by two wonderful EUV imagers, AIA and SUVI, that combine high-cadence, large-FOV, and multitemperature imagery, there are the following effects. First, the pre-eruptive structure in the source AR is special. The AR has very high magnetic flux densities (up to 5 kG; Wang et al. 2018) and contains a set of dense, bright loops reaching up to very large heights ($\gtrsim 0.5R_s$), as is indicated by their intense EUV emission in the temperature range 1–2 MK (see Figure 1). In the course of the eruption, this set of loops reconnects in the vertical current sheet. This means that high-density plasma is brought into the current sheet, forming the downward-closing flare loops, as well as the bright rim around the flux rope. From a general perspective, we expect that the mass that is brought into the cavity rim increases with the magnetic field strength, because the rate at which the field is brought into the reconnection region is proportional to the local Alfvén speed (Lin et al. 2004). High inflow speeds ($v \approx 100 \text{ km s}^{-1}$) into the reconnecting current sheet behind the rising flux rope have been reported for the event under study (Yan et al. 2018). Another phenomenon that may come into play is that, owing to the very strong fields involved and to the rapid expansion (and associated density depletion and adiabatic cooling), the cavity appears very dark. In addition, in the cooler AIA channels (where the bright rim around the cavity is not as distinct as in the hotter ones), the cavity yields a particularly high contrast against the bright set of surrounding loops that reaches high up into the corona.

As discussed in Lin et al. (2004), instead of the full hot rim around the erupting flux rope, more often U- or V-shaped structures are observed at the top of the current sheet, like in the 10% of white-light CMEs that are classified as disconnection events, or also observed by EUV imagers low in the corona (e.g., Régnier et al. 2011; Liu et al. 2013). The observations of U- or V-shaped structures suggest the existence of an organized flux-rope-like structure (see Vourlidis et al. 2013). The more frequent appearance of U- or V-shaped structures instead of a complete rim may be related to more moderate injection rates of the poloidal flux by magnetic reconnection (Lin et al. 2004). Another reason may be that in some events the field lines are not sufficiently strongly coiled around the flux rope. Only in the case of strongly coiled, i.e., dominantly poloidal fields, the field lines below the flux rope that come to reconnection are winding close to the apex of the flux rope, resulting in a high poloidal flux component of the freshly reconnected field that would manifest itself in a complete bright rim structure. In the more general case, the flux directly above the erupting flux rope (“strapping flux”) is also strongly sheared. When this flux comes to reconnection, it coils with a strong toroidal, i.e., shear, component around the erupting flux rope. This means that these fields manage to wind around the flux rope only far away from the apex, i.e., over the flux rope legs, resulting in V- or U-shaped structures of the hot plasma, when we observe along the axis of the flux rope. The formation of a complete rim in the present event suggests that the newly reconnected flux around

the flux rope is dominantly poloidal from the beginning of the event.

How do the structures of the eruption that we observe in the EUV connect to the traditional white-light coronagraph data? The composites of co-temporal SUVI/LASCO C2 difference images plotted in Figure 3 clearly show that the expanding CME shell observed in the SUVI 195 Å images fits to the CME front observed in the LASCO C2 data. In Figure 11 we plot a sequence of LASCO C2 and C3 direct images with less strong scaling to also obtain insight into the inner morphology of the white-light CME. In all four frames (as well as in later C3 images) we see a core with a bright rim-like structure embedded in the CME shell. In the C2 image at 16:12 UT, we can even see that this core has a teardrop shape, very similar to the cavity/rim morphology observed in the EUV (see Figure 2). To make sure that this white-light structure corresponds to the cavity/rim observed in the EUV, we extrapolated the cavity height and width kinematics derived from the SUVI and AIA EUV images to the LASCO FOV. Estimating the distance of the center of the cavity from the radial kinematics curve in Figure 8(a) (blue curve), we obtain a distance from the solar limb of $\approx 2.8R_s$ at 16:12 UT. This roughly fits with the distance of about $3.0R_s$ of the rim-like core observed in C2 at that time. We also cross-checked the correspondence of the width of the hot rim observed in EUV and the width of the rim observed in the white-light coronagraph images. Applying a linear fit to the evolution of the cavity width in Figure 8(a) (red curve) to the data after 14:53:30 UT, we obtain a mean expansion rate of about $0.041R_s$ per minute. Extrapolating this to the time 16:12 UT, where the rim-like structure is observed for the first time in LASCO C2, we obtain a width of $0.80R_s$. This is consistent with the width of the rim-like structure observed at that time in C2, which is about $(0.8\text{--}0.9)R_s$. Note that this correspondence also implies that in the LASCO FOV the overexpansion of the cavity has ceased and it is evolving almost self-similarly.

These findings imply that—in the present event—the core of the CME observed in the white-light coronagraphs is *not* a manifestation of the dense prominence plasma, as is the traditional view of the three-part CME structure, but it is a manifestation of dominantly poloidal flux and hot plasma continuously added around the expanding flux rope by the magnetic reconnection in the current sheet beneath. This is also consistent with the observations that in this event there is only little evidence for erupting prominence plasma, which dissolves already very early in the eruption (see Figure 2 and associated movie; see also Long et al. 2018). These findings strongly support the same conclusions in Lin et al. (2004) and Howard et al. (2017) and have important implications. First, the bright CME core observed in white-light coronagraph images is not necessarily a signature of an embedded prominence. Second, the cross section of the erupting flux rope can be significantly smaller than the CME cavity in white-light images, different from the widely accepted suggestion in Chen et al. (1997).

Finally, we note that the white-light CME evolution in Figure 11 (most obviously in the C3 images) shows a distinct deformation (“bulge”) of the outer CME front. This deformation is formed in the direction of motion of the expanding flux rope/cavity, which moves much faster than the outer CME shell, and is thus protruding from the bottom of the CME shell (see Figures 10(a), (b)). Such an accelerated motion of the flux rope with a speed considerably higher than that of the plasma

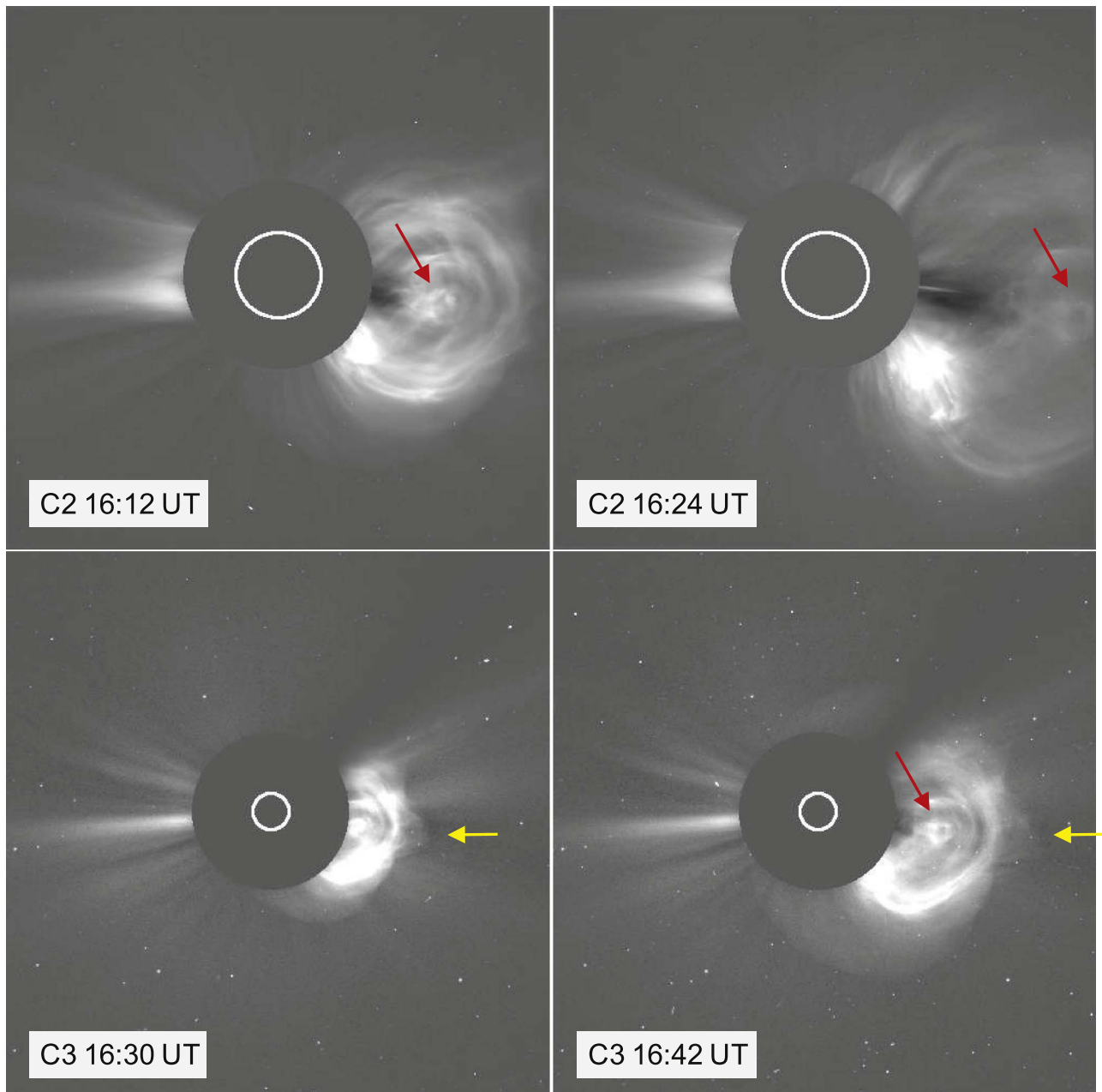


Figure 11. Sequence of LASC0 C2 (top) and C3 (bottom) images of the CME revealing the extension of the bright rim around the cavity as observed in the EUV into the white-light coronagraph data (indicated by red arrows). We also note a local deformation (“bulge”; indicated by yellow arrows) of the CME front/shock that is formed in the main direction of propagation of the flux rope (core), as it moves much faster than the outer CME shell (see Figure 10(b)).

overlying it causes a continuous compression of the magnetoplasma ahead of the flux rope, inevitably creating an MHD wave signal that propagates through the overlying CME structures, including the sheath region in front of the eruption. Since the speed of the driver is increasing (see Figure 10(b), red curve), each new element of the wave front has successively higher amplitude, implying that it propagates faster than the previous wave front elements (for the relationship between the driver kinematics and the wave front velocity profile and kinematics see Vrřnak & Lulić 2000). Thus, the new wave front elements sweep over the previous ones, overtaking them and heading toward the leading edge of the erupting structure. Finally, when the fastest elements reach the forehead of the structure, and continue the outward propagation faster than the flank elements of the erupting structure, the described effect

causes a local deformation of the shape of the overlying large-scale CME shell and the associated shock front in the form of a bulge. Such inhomogeneities and local regions of faster propagation speeds are a severe challenge and source of uncertainty in predictions of the arrival time/speed of the CME, its shock, and the space weather effects it produces (see also Török et al. 2018).

4.4. EUV Wave Formation

The associated EUV wave reveals high speeds, increasing with height from about 750 km s^{-1} at $0.05R_s$ to 1200 km s^{-1} at $0.5R_s$ above the solar limb. Such a behavior is also found in numerical simulations (e.g., Figure 6 in Vrřnak et al. 2016), and it is most likely related to the combination of two effects:

the ambient Alfvén speed increasing with height (Mann et al. 1999), and the flux rope overexpansion (e.g., Figure 2(c) in Vršnak et al. 2016). Toward the northern direction, the EUV wave can be distinguished from the driver (the CME flank) already at a distance as close as about 40 Mm at 15:52:24 UT. This is significantly smaller than typical distances of 100–200 Mm at which EUV and Moreton waves become observable (Warmuth et al. 2004; Kienreich et al. 2011; Muhr et al. 2014). As shown in the simulations in Vršnak et al. (2016), shock formation close to the contact surface implies a very impulsive acceleration of the driver. The early shock formation in this event is also supported by the associated metric type II burst, which starts at 15:53 UT (Gopalswamy et al. 2018). A fast acceleration of the piston results in a higher wave amplitude and speed of the wave crest, and consequently in formation of the shock in a shorter time/distance. This is fully consistent with our observations of an extremely fast lateral expansion of the CME with peak values up to 10 km s^{-2} and the formation of the EUV wave close to the CME flank during the rise of its impulsive acceleration. Toward the southern direction, the wave front can only later be distinguished from the CME flanks, which implies that the lateral expansion in this direction is not as impulsive as in the northern direction and/or that the ambient Alfvén speed is higher here, so the process of wave front steepening is slower.

The observations of the wave formation presented provide strong evidence for the interpretation of the global large-amplitude coronal EUV wave formation by a 3D piston mechanism (for the terminology and the physical background see, e.g., Vršnak 2005; Warmuth 2015). First, the wave speed is much higher than the speed of the expanding CME flank. This is a typical signature of the wave formation by the piston mechanism (see e.g., the simulation results presented in Figure 6(b) in Vršnak et al. 2016, showing that the wave is about two times faster than the piston), whereas in the case of a bow-shock scenario the speeds of the driver and the wave should be comparable (Vršnak 2005, and references therein). The higher speed of the wave as compared to the driver, indicative of a 3D piston mechanism, is well in line with the observations in the present case, where the CME flank expansion at different height levels is considerably slower than the EUV wave formed, by a factor of 2–3 (compare the blue and black lines outlining the CME flank and EUV wave propagation in the stack plots in Figure 9). Second, according to simulations presented in Vršnak et al. (2016), at low coronal heights (at the height of the flux rope center), the wave is formed and first appears during the impulsive lateral expansion of the magnetic structure, i.e., close in time to the CME peak acceleration and spatially close to its “contact surface” (see Figures 6(a), (b) therein, and the supporting observations in Patsourakos et al. 2010a and Cheng et al. 2012). This is in good correspondence with the distance/time we find in the observations of the event under study: 15:52:30 UT corresponds to the impulsive lateral acceleration phase of the CME shell, where the lateral acceleration has already reached a value as high as 6 km s^{-2} , and the impulsive decrease of the CME aspect ratio. Finally, we note that in the observations we identify a transient dimming traveling behind the wave front (Figure 1 and associated movie), which is expected in the case of wave formation due to the 2D and/or 3D piston mechanism (Landau & Lifshitz 1987; Vršnak et al. 2016).

Interestingly, despite the strength, high speed, and global propagation of this EUV wave (see also Liu et al. 2018), it did

not reveal any signature of an associated Moreton wave. This means that the pressure pulse initiated by the coronal wave was not strong enough to sufficiently perturb the underlying denser chromospheric plasma (e.g., Vršnak et al. 2016). This is probably due to the fact that in the present case the main lateral CME expansion—although very strong and impulsive (with a peak acceleration of 10 km s^{-2})—happened at a comparatively large height and started from a large source region. Finally, we note that this event was associated with a widespread SEP event, covering $>230^\circ$ in heliolongitude (Guo et al. 2018). We may speculate that the formation of these widespread SEPs is also related to the extremely impulsive lateral expansion of the CME and the associated coronal shock formation close to the Sun.

5. Conclusions

The CME associated with the X8.2 flare of 2017 September 10 provides us with unique observations on the genesis, magnetic morphology, and impulsive dynamical evolution of a very fast solar eruption. In this event, the different parts of the CME can be clearly identified and followed in multitemperature EUV images and uniquely associated with the morphology in the white-light coronagraph data.

We clearly demonstrate that the hot bright rim observed around the quickly expanding EUV cavity is formed by the dominantly poloidal flux and the attached heated plasma that is added to the erupting flux rope by magnetic reconnection in the large-scale current sheet beneath, and that this structure extends into the coronagraph FOV as the CME core. These findings corroborate the recently suggested rethinking of the traditional view on the three-part CME morphology, which interprets the CME core as the signature of the erupting flux rope, rather than as the signature of prominence material trapped in the bottom part of the flux rope. Further studies are needed to quantify in what fraction of CMEs the core is a manifestation of the prominence and/or of the reconnected poloidal flux and plasma, and how we can use these observations to obtain estimates of the poloidal flux supplied to the eruption by magnetic reconnection and sustaining its acceleration. Our findings also imply that the cross section of the erupting flux rope can be significantly smaller than the CME cavity observed in white-light images.

In the present event, the clearly defined CME structures, together with the high-cadence large-FOV EUV imagery, also allowed us to derive the impulsive dynamics separately for the radial and lateral expansions of both the CME shell and the flux rope, all of which revealed extreme acceleration values with peaks in the range of $5\text{--}10 \text{ km s}^{-1}$. The much higher radial propagation speed of the flux rope as compared to the CME shell is identified to be the reason for the substantial deformation of the white-light CME front and shock in the form of a faster-moving bulge. Such local inhomogeneities have important implications for space weather forecasts, as they pose additional difficulties in the prediction of the CME arrival time and speed at Earth. Finally, we note that both the CME shell and the flux rope exhibit a strong lateral overexpansion during the impulsive phase of the event. The overexpansion and the 2D/3D piston mechanism are essential for generating the fast and globally propagating EUV wave associated.

A.M.V., K.D., and M.T. acknowledge the Austrian Science Fund (FWF): P24092-N16, P27292-N20, and the Austrian Space Applications Programme of the Austrian Research

Promotion Agency FFG (ASAP-11 4900217). B.V. acknowledges financial support by the Croatian Science Foundation under the project 6212 *Solar and Stellar Variability*. B.K. acknowledges support by the DFG. D.M.L. received support from the European Commission's H2020 Programme under the following grant agreements: GRESt (no. 653982) and Pre-EST (no. 739500).

Facilities: GOES, RHESSI, SOHO.

ORCID iDs

Astrid M. Veronig  <https://orcid.org/0000-0003-2073-002X>
Tatiana Podladchikova  <https://orcid.org/0000-0002-9189-1579>

Karin Dissauer  <https://orcid.org/0000-0001-5661-9759>
Manuela Temmer  <https://orcid.org/0000-0003-4867-7558>
Daniel B. Seaton  <https://orcid.org/0000-0002-0494-2025>

David Long  <https://orcid.org/0000-0003-3137-0277>

Louise Harra  <https://orcid.org/0000-0001-9457-6200>

Bernhard Kliem  <https://orcid.org/0000-0002-5740-8803>

References

- Bak-Stejslicka, U., Kołomański, S., & Mrozek, T. 2013, *SoPh*, **283**, 505
Bein, B. M., Berkebile-Stoiser, S., Veronig, A. M., et al. 2011, *ApJ*, **738**, 191
Berkebile-Stoiser, S., Veronig, A. M., Bein, B. M., & Temmer, M. 2012, *ApJ*, **753**, 88
Brueckner, G. E., Howard, R. A., Koomen, M. J., et al. 1995, *SoPh*, **162**, 357
Chen, J. 1989, *ApJ*, **338**, 453
Chen, J., Howard, R. A., Brueckner, G. E., et al. 1997, *ApJL*, **490**, L191
Chen, P. F., & Wu, Y. 2011, *ApJL*, **732**, L20
Cheng, X., Guo, Y., & Ding, M. 2017, *SciChE*, **60**, 1383
Cheng, X., Li, Y., Wan, L. F., et al. 2018, *ApJ*, **866**, 64
Cheng, X., Zhang, J., Ding, M. D., Liu, Y., & Poomvises, W. 2013, *ApJ*, **763**, 43
Cheng, X., Zhang, J., Liu, Y., & Ding, M. D. 2011, *ApJL*, **732**, L25
Cheng, X., Zhang, J., Olmedo, O., et al. 2012, *ApJL*, **745**, L5
Dere, K. P., Brueckner, G. E., Howard, R. A., Michels, D. J., & Delaboudiniere, J. P. 1999, *ApJ*, **516**, 465
Dissauer, K., Veronig, A. M., Temmer, M., Podladchikova, T., & Vanninathan, K. 2018, *ApJ*, **863**, 169
Dresing, N., Gómez-Herrero, R., Heber, B., et al. 2014, *A&A*, **567**, A27
Dresing, N., Gómez-Herrero, R., Klassen, A., et al. 2012, *SoPh*, **281**, 281
Emslie, A. G., Dennis, B. R., Shih, A. Y., et al. 2012, *ApJ*, **759**, 71
Fletcher, L., Dennis, B. R., Hudson, H. S., et al. 2011, *SSRv*, **159**, 19
Forbes, T. G., Linker, J. A., Chen, J., et al. 2006, *SSRv*, **123**, 251
Gary, D. E., Chen, B., Dennis, B. R., et al. 2018, *ApJ*, **863**, 83
Gary, G. A. 2001, *SoPh*, **203**, 71
Gibson, S. E., Foster, D., Burkepile, J., de Toma, G., & Stanger, A. 2006, *ApJ*, **641**, 590
Gibson, S. 2015, *ASSL*, **415**, 323
Gómez-Herrero, R., Dresing, N., Klassen, A., et al. 2015, *ApJ*, **799**, 55
Gonzalez, W. D., Joselyn, J. A., Kamide, Y., et al. 1994, *JGR*, **99**, 5771
Gopalswamy, N., Yashiro, S., Mäkelä, P., et al. 2018, *ApJL*, **863**, L39
Gopalswamy, N., Yashiro, S., Michalek, G., et al. 2009, *EM&P*, **104**, 295
Goryaev, F. F., Slemzin, V. A., Rodkin, D. G., et al. 2018, *ApJL*, **856**, L38
Green, L. M., Török, T., Vršnak, B., Manchester, W., & Veronig, A. 2018, *SSRv*, **214**, 46
Guo, J., Dumbović, M., Wimmer-Schweingruber, R. F., et al. 2018, *SpWea*, **16**, 1156
Howard, T. A., DeForest, C. E., Schneck, U. G., & Alden, C. R. 2017, *ApJ*, **834**, 86
Hudson, H. S., Lemen, J. R., & Webb, D. F. 1997, in ASP Conf. Ser. 111, *Magnetic Reconnection in the Solar Atmosphere*, ed. R. D. Bentley & J. T. Mariska (San Francisco, CA: ASP), 379
Illing, R. M. E., & Hundhausen, A. J. 1986, *JGR*, **91**, 10951
Kienreich, I. W., Veronig, A. M., Muhr, N., et al. 2011, *ApJL*, **727**, L43
Kliem, B., Forbes, T. G., Patsourakos, S., & Vourlidas, A. 2014, AAS Meeting, **224**, 212.06
Koskinen, H. E. J., Baker, D. N., Balogh, A., et al. 2017, *SSRv*, **212**, 1137
Landau, L. D., & Lifshitz, E. M. 1987, *Fluid Mechanics* (2nd ed.; Oxford: Pergamon)
Lario, D., Kwon, R.-Y., Vourlidas, A., et al. 2016, *ApJ*, **819**, 72
Lemen, J. R., Title, A. M., Akin, D. J., et al. 2012, *SoPh*, **275**, 17
Li, Y., Xue, J. C., Ding, M. D., et al. 2018, *ApJL*, **853**, L15
Lin, J., Raymond, J. C., & van Ballegooijen, A. A. 2004, *ApJ*, **602**, 422
Lin, R. P., Dennis, B. R., Hurford, G. J., et al. 2002, *SoPh*, **210**, 3
Liu, W., Chen, Q., & Petrosian, V. 2013, *ApJ*, **767**, 168
Liu, W., Jin, M., Downs, C., et al. 2018, *ApJL*, **864**, L24
Liu, W., & Ofman, L. 2014, *SoPh*, **289**, 3233
Long, D. M., Bloomfield, D. S., Chen, P. F., et al. 2017, *SoPh*, **292**, 7
Long, D. M., Harra, L. K., Matthews, S. A., et al. 2018, *ApJ*, **855**, 74
Low, B. C., & Hundhausen, J. R. 1995, *ApJ*, **443**, 818
Lulić, S., Vršnak, B., Žic, T., et al. 2013, *SoPh*, **286**, 509
Mann, G., Klassen, A., Estel, C., & Thompson, B. J. 1999, in ESA Special Publication 446, 8th SOHO Workshop: Plasma Dynamics and Diagnostics in the Solar Transition Region and Corona, ed. J.-C. Vial & B. Kaldeich-Schumann (Paris: ESA), 477
Morgan, H., & Druckmüller, M. 2014, *SoPh*, **289**, 2945
Muhr, N., Veronig, A. M., Kienreich, I. W., et al. 2014, *SoPh*, **289**, 4563
Muhr, N., Veronig, A. M., Temmer, M., Kienreich, I., & Vršnak, B. 2011, *ApJ*, **739**, 89
Neupert, W. M., Thompson, B. J., Gurman, J. B., & Plunkett, S. P. 2001, *JGR*, **106**, 25215
Nindos, A., Patsourakos, S., Vourlidas, A., & Tagikas, C. 2015, *ApJ*, **808**, 117
Omodei, N., Pesce-Rollins, M., Longo, F., Allafort, A., & Krucker, S. 2018, *ApJL*, **865**, L7
Pagano, P., Mackay, D. H., & Poedts, S. 2013, *A&A*, **560**, A38
Patsourakos, S., & Vourlidas, A. 2012, *SoPh*, **281**, 187
Patsourakos, S., Vourlidas, A., & Kliem, B. 2010a, *A&A*, **522**, A100
Patsourakos, S., Vourlidas, A., & Stenborg, G. 2010b, *ApJL*, **724**, L188
Pesnelli, W. D., Thompson, B. J., & Chamberlin, P. C. 2012, *SoPh*, **275**, 3
Podladchikova, T., Van der Linden, R., & Veronig, A. M. 2017, *ApJ*, **850**, 81
Régnier, S., Walsh, R. W., & Alexander, C. E. 2011, *A&A*, **533**, L1
Schwenn, R., dal Lago, A., Huttunen, E., & Gonzalez, W. D. 2005, *AnGeo*, **23**, 1033
Seaton, D. B., & Darnel, J. M. 2018, *ApJL*, **852**, L9
Shafranov, V. D. 1966, *RvPP*, **2**, 103
St. Cyr, O. C., Burkepile, J. T., Hundhausen, A. J., & Lecinski, A. R. 1999, *JGR*, **104**, 12493
Temmer, M., Veronig, A. M., Kontar, E. P., Krucker, S., & Vršnak, B. 2010, *ApJ*, **712**, 1410
Temmer, M., Veronig, A. M., Vršnak, B., et al. 2008, *ApJL*, **673**, L95
Temmer, M., Vršnak, B., Žic, T., & Veronig, A. M. 2009, *ApJ*, **702**, 1343
Török, T., Downs, C., Linker, J. A., et al. 2018, *ApJ*, **856**, 75
Tsurutani, B. T., Gonzalez, W. D., Tang, F., Akasofu, S. I., & Smith, E. J. 1988, *JGR*, **93**, 8519
Tsurutani, B. T., Gonzalez, W. D., Tang, F., & Lee, Y. T. 1992, *GeoRL*, **19**, 73
Veronig, A. M., Muhr, N., Kienreich, I. W., Temmer, M., & Vršnak, B. 2010, *ApJL*, **716**, L57
Veronig, A. M., Temmer, M., & Vršnak, B. 2008, *ApJL*, **681**, L113
Vourlidas, A., Howard, R. A., Esfandiari, E., et al. 2010, *ApJ*, **722**, 1522
Vourlidas, A., Lynch, B. J., Howard, R. A., & Li, Y. 2013, *SoPh*, **284**, 179
Vourlidas, A., Wu, S. T., Wang, A. H., Subramanian, P., & Howard, R. A. 2003, *ApJ*, **598**, 1392
Vršnak, B. 2005, *EOSTr*, **86**, 112
Vršnak, B. 2008, *AnGeo*, **26**, 3089
Vršnak, B. 2016, *AN*, **337**, 1002
Vršnak, B., & Lulić, S. 2000, *SoPh*, **196**, 157
Vršnak, B., Maričić, D., Stanger, A. L., et al. 2007, *SoPh*, **241**, 85
Vršnak, B., Maričić, D., Stanger, A. L., & Veronig, A. 2004, *SoPh*, **225**, 355
Vršnak, B., Žic, T., Lulić, S., Temmer, M., & Veronig, A. M. 2016, *SoPh*, **291**, 89
Wang, H., Yurchyshyn, V., Liu, C., et al. 2018, *RNAAS*, **2**, 8
Warmuth, A. 2015, *LRSP*, **12**, 3
Warmuth, A., Vršnak, B., Magdalenic, J., Hanslmeier, A., & Otruba, W. 2004, *A&A*, **418**, 1101
Warren, H. P., Brooks, D. H., Ugarte-Urra, I., et al. 2018, *ApJ*, **854**, 122
Williams, D. R., Török, T., Démoulin, P., van Driel-Gesztelyi, L., & Kliem, B. 2005, *ApJL*, **628**, L163
Yan, X. L., Yang, L. H., Xue, Z. K., et al. 2018, *ApJL*, **853**, L18
Ying, B., Feng, L., Lu, L., et al. 2018, *ApJ*, **856**, 24
Zarro, D. M., Sterling, A. C., Thompson, B. J., Hudson, H. S., & Nitta, N. 1999, *ApJL*, **520**, L139
Zhang, J., Cheng, X., & Ding, M.-D. 2012, *NatCo*, **3**, 747
Zhang, J., & Dere, K. P. 2006, *ApJ*, **649**, 1100
Zhang, J., Dere, K. P., Howard, R. A., Kundu, M. R., & White, S. M. 2001, *ApJ*, **559**, 452